Available online at www.sciencedirect.com
SCIENCE DIRECT®
Journal of Computational Physics 213 (2006) 413–436
JOURNAL OF COMPUTATIONAL PHYSICS
www.elsevier.com/locate/jcp

An adaptive local deconvolution method for implicit LES

Stefan Hickel [a,*], Nikolaus A. Adams [a], J. Andrzej Domaradzki [b]

[a] Technische Universität München, Institute of Aerodynamics, Bolzmannstrasse 15, D-85747 Garching, Germany
[b] University of Southern California, Department of Aerospace and Mechanical Engineering, Los Angeles, CA 90089-1191, USA

Received 11 March 2005; received in revised form 19 July 2005; accepted 17 August 2005
Available online 27 September 2005

Abstract

The adaptive local deconvolution method (ALDM) is proposed as a new nonlinear discretization scheme designed for implicit large-eddy simulation (ILES) of turbulent flows. In ILES the truncation error of the discretization of the convective terms functions as a subgrid-scale model. Therefore, the model is implicitly contained within the discretization, and an explicit computation of model terms becomes unnecessary. The discretization is based on a solution-adaptive deconvolution operator which allows to control the truncation error. Deconvolution parameters are determined by an analysis of the spectral numerical viscosity. An automatic optimization based on an evolutionary algorithm is employed to obtain a set of parameters which results in an optimum spectral match for the numerical viscosity with theoretical predictions for isotropic turbulence. Simulations of large-scale forced and decaying three-dimensional homogeneous isotropic turbulence show an excellent agreement with theory and experimental data and demonstrate the good performance of the implicit model. As an example for transitional flows, instability and breakdown of the three-dimensional Taylor–Green vortex are considered. The implicit model correctly predicts instability growth and transition to developed turbulence. It is shown that the implicit model performs at least as well as established explicit models.

AMS: 65M99; 76F65; 76M25

Keywords: Implicit large-eddy simulation; Subgrid-scale modeling; Deconvolution; Isotropic turbulence; Taylor–Green vortex

1. Introduction

In large-eddy simulation (LES) of turbulent flows the evolution of non-universal larger scales is computed, whereas their interaction with universal smaller scales is modeled. The precise definition of large scales varies from one approach to another. Common numerical discretization methods such as finite-volume or finite-difference schemes represent the continuous solution by grid functions at discrete time instants. This approximation amounts to the removal of spatial and temporal scales which cannot be resolved by the grid functions.

* Corresponding author. Tel.: +49 89 289 16135; fax: +49 89 289 16139.
E-mail addresses: sh@tum.de (S. Hickel), nikolaus.adams@tum.de (N.A. Adams), jad@usc.edu (J.A. Domaradzki).

0021-9991/$ - see front matter
doi:10.1016/j.jcp.2005.08.017

For the purpose of eliminating small scales, a spatial low-pass filter operation was suggested by Leonard [1]. It is based on the convolution

$$\bar{\varphi}(\boldsymbol{x},t) = \boldsymbol{G}(\boldsymbol{x}) * \varphi(\boldsymbol{x},t), \tag{1}$$

where $\boldsymbol{G}(\boldsymbol{x})$ is a filter kernel with normalization $\iiint \boldsymbol{G}(\boldsymbol{x})\,\mathrm{d}\boldsymbol{x} = 1$. An overbar denotes the resolved-scale component of a function φ. The unresolved-scale component results from $\varphi\prime = \varphi - \bar{\varphi}$. More generally, a spatial and temporal filter can be considered, see [2,3]. Since spatial and temporal scales are coupled through the underlying transport equation it is common practice to consider spatial filtering only, assuming that all relevant temporal scales are resolved by choosing the time-step small enough. For a converse approach and recent developments on temporal filtering we refer to [4,5].

We consider incompressible turbulent flows which are governed by the Navier–Stokes equation in non-dimensional form

$$\frac{\partial \boldsymbol{u}}{\partial t} + \boldsymbol{\nabla}\cdot\boldsymbol{F} + \boldsymbol{\nabla}p - \nu\boldsymbol{\nabla}\cdot\boldsymbol{\nabla}\boldsymbol{u} = \boldsymbol{0}, \tag{2}$$

where $\boldsymbol{u} = [u,v,w]$ is the velocity, $\boldsymbol{F} = \boldsymbol{u}\boldsymbol{u}$ is the nonlinear convection term, and ν is the molecular viscosity. The pressure p serves as a scalar field to satisfy the incompressible continuity equation

$$\boldsymbol{\nabla}\cdot\boldsymbol{u} = 0. \tag{3}$$

The nonlinearity enters the pressure through the Poisson equation

$$\boldsymbol{\nabla}\cdot\boldsymbol{\nabla}p = -\boldsymbol{\nabla}\cdot\boldsymbol{\nabla}\cdot\boldsymbol{F}, \tag{4}$$

which has to be accounted for in subgrid-scale (SGS) modeling. We collect all nonlinear terms in

$$\boldsymbol{\nabla}\cdot\boldsymbol{N}(\boldsymbol{u}) = \boldsymbol{\nabla}\cdot\boldsymbol{F}(\boldsymbol{u}) + \boldsymbol{\nabla}p. \tag{5}$$

The differential equations for the resolved scales are obtained by applying the filter (1) to Eqs. (2) and (3):

$$\frac{\partial \bar{\boldsymbol{u}}_N}{\partial t} + \boldsymbol{G} * \boldsymbol{\nabla}\cdot\boldsymbol{N}_N(\boldsymbol{u}_N) - \nu\boldsymbol{\nabla}\cdot\boldsymbol{\nabla}\bar{\boldsymbol{u}}_N = -\boldsymbol{G} * \boldsymbol{\nabla}\cdot\boldsymbol{\tau}_{\mathrm{SGS}}, \tag{6a}$$

$$\boldsymbol{\nabla}\cdot\bar{\boldsymbol{u}}_N = 0. \tag{6b}$$

At this point it should be noted that Leonard's ansatz implies a *subsequent* discretization of the filtered equations. The subscript N indicates the grid functions obtained by projecting continuous functions onto the numerical grid. This projection corresponds to an additional filtering in Fourier space with cut-off at the Nyquist wavenumber $\xi_N = \pi/\Delta$, where Δ is a constant grid spacing.

In Eq. (6), the represented-scale part of the unfiltered field is reconstructed for computing the nonlinear term [6]. This can be accomplished by an inverse-filter operation $\boldsymbol{u}_N = \boldsymbol{G}^{-1} * \bar{\boldsymbol{u}}_N$ applied to represented scales. Since non-represented scales cannot be recovered it is $\boldsymbol{u}_N \neq \boldsymbol{u}$, which results in the subgrid-stress tensor

$$\boldsymbol{\tau}_{\mathrm{SGS}} = \boldsymbol{N}(\boldsymbol{u}) - \boldsymbol{N}_N(\boldsymbol{u}_N). \tag{7}$$

For a closure of Eq. (6) the subgrid-stress tensor (7) has to be approximated by a model. Numerous approaches to derive model closures have been pursued since Smagorinsky's eddy-viscosity model. We refer to these closures as *explicit* models. Comprehensive reviews are available in the textbooks of Sagaut [7] and Lesieur [8].

The filter concept of Leonard is commonly employed for deriving SGS models without reference to a computational grid and without taking into account a discretization scheme. However, when numerically solving Eq. (6) the explicitly computed SGS stress is affected by the truncation error of the discretization scheme. This interference can result in strange results such as the lack of grid convergence. Ghosal [9] has analyzed this problem analytically and finds that the truncation error even of a fourth-order central-difference discretization can have the same order of magnitude as the SGS stress. With implicit large-eddy simulation (ILES) this interference between truncation error and SGS stress is exploited. Instead of an explicit computation of the SGS stress, the truncation error of the discretization scheme itself is employed to model the effects of unresolved scales. Due to numerical approximations the exact solution of the discrete equations does not satisfy Eq. (6) with $\boldsymbol{\tau}_{\mathrm{SGS}} = \boldsymbol{0}$, but rather a modified differential equation (MDE). For a general implicit SGS model, as implied by a general LES discretization scheme, this MDE is given by:

$$\frac{\partial \bar{\boldsymbol{u}}_N}{\partial t} + \widetilde{\boldsymbol{G}} * \widetilde{\boldsymbol{\nabla}} \cdot \widetilde{\boldsymbol{N}}_N(\widetilde{\boldsymbol{u}}_N) - \nu \boldsymbol{\nabla} \cdot \boldsymbol{\nabla} \bar{\boldsymbol{u}}_N = \boldsymbol{0}, \tag{8a}$$

$$\boldsymbol{\nabla} \cdot \bar{\boldsymbol{u}}_N = 0. \tag{8b}$$

In the following we consider a top-hat filter-kernel $\boldsymbol{G}$, see Eq. (11). For this filter kernel, the LES equations (6) evaluated on a grid correspond to a finite-volume discretization, and $\widetilde{\boldsymbol{u}}_N$ denotes an approximant of the velocity $\boldsymbol{u}_N$. The local Riemann problem is approximated by a consistent numerical flux function $\widetilde{\boldsymbol{F}}_N$ which yields the divergence-free nonlinear term $\widetilde{\boldsymbol{N}}_N$. The symbols $\widetilde{\boldsymbol{G}} * \widetilde{\boldsymbol{\nabla}}$ indicate that $\boldsymbol{G}$ and $\boldsymbol{\nabla}$ are replaced by their respective numerical approximations. In fact $\widetilde{\boldsymbol{G}} * \widetilde{\boldsymbol{\nabla}}$ can be a nonlinear operator. The truncation error due to the discretization of the convective term is accordingly

$$\mathscr{G}_N = \boldsymbol{G} * \boldsymbol{\nabla} \cdot \boldsymbol{N}_N(\boldsymbol{u}_N) - \widetilde{\boldsymbol{G}} * \widetilde{\boldsymbol{\nabla}} \cdot \widetilde{\boldsymbol{N}}_N(\widetilde{\boldsymbol{u}}_N). \tag{9}$$

We point out that the effect of the truncation error of the diffusive flux could also be considered, as was done by Zandonade et al. [10] for finite-volume optimal LES. This approach, however, can lead to Reynolds-number dependent model coefficients and is therefore undesirable. We employ standard high-order centered schemes for discretizing the diffusive flux. Their contribution to the implicit model is negligible even for rather small Reynolds numbers as will be shown in Section 4.

For implicit SGS modeling, the discretization scheme has to be specifically designed so that the truncation error $\mathscr{G}_N$ has physical significance. A numerical analysis of Garnier et al. [11] deals with several approaches to implicit LES and demonstrates the difficulties in satisfying this requirement. It was found that artificial dissipation introduced by the most common nonlinearly stable discretizations indeed stabilizes under-resolved turbulence simulations. For the investigated schemes, however, small scales suffer from excessive numerical damping such that the probability-density functions of velocity increments and pressure exhibit the typical behavior of low Reynolds-number flows rather than that of high Reynolds-number turbulence. Thus, it appears that for these schemes the prediction accuracy of subgrid effects is poor, although some general trends were reproduced. A more recent review by Grinstein and Fureby [12], however, emphasizes the potential of implicit LES for flows in complex geometries.

An approach similar to the idea of implicit SGS modeling is pursued by Zandonade et al. [10] where stochastic estimation is adapted to derive various linear (i.e., constant coefficient) finite-volume discretizations which are statistically optimal for isotropic turbulence. Since for this kind of discretizations the SGS model is provided by the discrete convective and diffusive fluxes they also qualify as implicit LES schemes. A drawback of this approach is that solution adaptivity cannot be accomplished within the framework of [10].

In the present paper, we extend our initial work on bridging numerical discretization and SGS modeling [13] to fluid-flow turbulence. For this purpose, we develop systematic procedures for design and analysis of discretization schemes. An important tool is the modified-differential equation analysis (MDEA) [13–15]. Based on Taylor series expansions of the solution, MDEA allows to analyze the relation of the implicit model to a given explicit SGS model. The numerical truncation error, i.e., the implicit SGS model, resembles an explicit SGS model if the filtered divergence of the model SGS tensor in Eq. (6) is approximated

$$\mathscr{G}_N \approx -\boldsymbol{G} * \boldsymbol{\nabla} \cdot \boldsymbol{\tau}_{\mathrm{SGS}}. \tag{10}$$

Linear discretization schemes for linear differential equations can be analyzed in Fourier space with the modified-wavenumber concept (e.g. [16]). A spectral analysis is well suited for isotropic turbulence for which theoretical models are usually formulated in spectral space [8,17]. MDEA of more complicated nonlinear discretization schemes of nonlinear three-dimensional differential equations becomes tedious. An alternative approach follows the method of Domaradzki et al. [18], where the spectral numerical viscosity is considered which can be matched to a given explicit SGS model or to theoretical models.

An approach to implicit LES based on deconvolution methods was recently proposed by Adams, Hickel & Franz [13]. We refer to this approach as the *adaptive local deconvolution method* (ALDM). For ALDM, a local approximation of the deconvolved velocity field is obtained from a solution-adaptive combination of approximation polynomials. In Eq. (8a), the interpolant $\widetilde{\boldsymbol{u}}_N$ denotes the approximately deconvolved $\bar{\boldsymbol{u}}_N$. Free parameters involved in the approximate deconvolution operator allow for implicit SGS modeling. The efficiency of this approach was demonstrated in [13] for 1D conservation laws on the example of the viscous Burgers equation. In this paper, we develop the ALDM approach for three spatial dimensions and the Navier–Stokes

equations. A comprehensive formulation is given in Section 2. The derivation of the implicit SGS model is detailed in Section 3. Optimal parameters are identified by an automatic optimization employing an evolutionary algorithm. Computational experiments for transitional and fully turbulent flows for validation of the implicit model are presented in Section 4. We do not consider wall-bounded flows in this paper since the main purpose is the development of the general method. The near-wall region of turbulent flows requires a somewhat different analysis for implicit modeling. This analysis and results for wall-bounded flows are subject of ongoing research and will be reported in a separate paper.

2. The adaptive local deconvolution method

The adaptive local deconvolution method (ALDM) is a nonlinear discretization scheme designed for implicit LES. ALDM is based on standard approaches which, however, are modified in such a way that the resulting truncation error functions as implicit SGS model. The essential building blocks are:

1. an adaptive local deconvolution operator $\widetilde{\boldsymbol{G}}^{-1}$ that returns $\widetilde{\boldsymbol{u}}_N = \widetilde{\boldsymbol{G}}^{-1} * \bar{\boldsymbol{u}}_N$,
2. a numerical flux function $\widetilde{\boldsymbol{F}}_N$,
3. a numerical integration and differentiation scheme $\widetilde{\boldsymbol{G}} * \widetilde{\boldsymbol{\nabla}}$ approximating $\boldsymbol{G} * \boldsymbol{\nabla}$.

In the following, we develop a general nonlinear discretization scheme, which is as simple as possible to facilitate computation and as complex as necessary to allow for implicit modeling.

2.1. Filter and differentiation operator

With ALDM we consider the discretized equations directly as proposed by Schumann [19]. Although filtering is not performed explicitly we can use the filter formulation of Leonard as analytical tool when designing and analyzing the discrete operators. The framework is a finite-volume discretization with the top-hat filter

$$\boldsymbol{G}(\boldsymbol{x}_{i,j,k}, \boldsymbol{x}) = \frac{1}{\Delta x_i \Delta y_j \Delta z_k} \begin{cases} 1, & (\boldsymbol{x}_{i,j,k} + \boldsymbol{x}) \in I_{i,j,k}, \\ 0, & \text{otherwise}, \end{cases} \tag{11}$$

which returns the cell average of a function

$$\bar{\varphi}(\boldsymbol{x}_{i,j,k}, t) = \frac{1}{\Delta x_i \Delta y_j \Delta z_k} \int\int\int_{I_{i,j,k}} \varphi(\boldsymbol{x}_{i,j,k} - \boldsymbol{x}, t)\, \mathrm{d}\boldsymbol{x}. \tag{12}$$

The integration domain

$$I_{i,j,k} = \left[x_{i-\frac{1}{2}}, x_{i+\frac{1}{2}}\right] \times \left[y_{j-\frac{1}{2}}, y_{j+\frac{1}{2}}\right] \times \left[z_{k-\frac{1}{2}}, z_{k+\frac{1}{2}}\right] \tag{13}$$

is equivalent to a cell of the underlying Cartesian computational grid so that the filter width corresponds to the local grid size

$$\Delta \boldsymbol{x}_{i,j,k} = \begin{bmatrix} \Delta x_i \\ \Delta y_j \\ \Delta z_k \end{bmatrix} = \begin{bmatrix} x_{i+1/2} - x_{i-1/2} \\ y_{j+1/2} - y_{j-1/2} \\ z_{k+1/2} - z_{k-1/2} \end{bmatrix}. \tag{14}$$

Here and in the following half-integer indices denote cell faces.

For implicit SGS modeling we only consider the nonlinear term $\boldsymbol{N}(\boldsymbol{u})$ in the momentum equation (2), whereas the linear terms, i.e., the diffusive flux, are approximated by a standard centered discretization. By Gauss' and Green's theorems filtering applied to the flux divergence $\boldsymbol{\nabla} \cdot \boldsymbol{N}(\boldsymbol{u})$ returns the flux through the surface $S_{i,j,k}$ of cell $I_{i,j,k}$

$$[\boldsymbol{G} * \boldsymbol{\nabla} \cdot \boldsymbol{N}(\boldsymbol{u})]_{i,j,k} = \int\int_{S_{i,j,k}} \boldsymbol{n} \cdot \boldsymbol{F}\, \mathrm{d}S + \int\int_{S_{i,j,k}} \boldsymbol{n} p\, \mathrm{d}S, \tag{15}$$

where $\boldsymbol{n}$ is the unit normal vector on the cell faces. ALDM applies to the convective flux $\boldsymbol{F} = \boldsymbol{uu}$. For incompressible flows, the normal stresses due to the pressure p are subsequently computed solving a Poisson equation (4). Evaluating the convective integral in Eq. (15) we obtain

$$\int\int_{S_{i,j,k}} \boldsymbol{n}\cdot\boldsymbol{F}\,\mathrm{d}S = \frac{1}{\Delta x_i}\left({}^1\bar{\boldsymbol{f}}(x_{i+\frac{1}{2}},y_j,z_k) - {}^1\bar{\boldsymbol{f}}(x_{i-\frac{1}{2}},y_j,z_k)\right) + \frac{1}{\Delta y_j}\left({}^2\bar{\boldsymbol{f}}(x_i,y_{j+\frac{1}{2}},z_k) - {}^2\bar{\boldsymbol{f}}(x_i,y_{j-\frac{1}{2}},z_k)\right) + \frac{1}{\Delta z_k}\left({}^3\bar{\boldsymbol{f}}(x_i,y_j,z_{k+\frac{1}{2}}) - {}^3\bar{\boldsymbol{f}}(x_i,y_j,z_{k-\frac{1}{2}})\right). \tag{16}$$

The flux vector ${}^l\boldsymbol{f} = u_l\boldsymbol{u}$ denotes the l-direction component of $\boldsymbol{F}$ and ${}^l\bar{\boldsymbol{f}}$ is the spatial average of ${}^l\boldsymbol{f}$ over the cell face with $n_l = \pm 1$. Here and in the following the coordinate system $\{x,y,z\}$ is synonymous with $\{1,2,3\}$.

The numerical computation of ${}^l\bar{\boldsymbol{f}}$ involves approximations which we explain now on the example of the flux in z-direction

$${}^3\bar{\boldsymbol{f}}(x_i,y_j,z_{k+\frac{1}{2}}) = \frac{1}{\Delta x\Delta y}\int_{x_{i-\frac{1}{2}}}^{x_{i+\frac{1}{2}}}\int_{y_{j-\frac{1}{2}}}^{y_{j+\frac{1}{2}}} {}^3\boldsymbol{f}(x,y,z_{k+\frac{1}{2}})\,\mathrm{d}x\,\mathrm{d}y. \tag{17}$$

A Gaussian quadrature rule with $(2m+1)^2$ numerical integration points returns

$${}^3\bar{\boldsymbol{f}}(x_i,y_j,z_{k+\frac{1}{2}}) \doteq \sum_{\alpha=1}^{2m+1}\sum_{\beta=1}^{2m+1} C_{\alpha\beta}\,{}^3\boldsymbol{f}(x_{i+\alpha-n},y_{j+\beta-n},z_{k+\frac{1}{2}}). \tag{18}$$

Our present computational implementation allows for two different integration schemes with 3^2 nodes, given by

$$\boldsymbol{C}_2 = \begin{bmatrix} 0 & 0 & 0 \\ 0 & 1 & 0 \\ 0 & 0 & 0 \end{bmatrix} \quad \text{and} \quad \boldsymbol{C}_4 = \frac{1}{24}\begin{bmatrix} 0 & 1 & 0 \\ 1 & 20 & 1 \\ 0 & 1 & 0 \end{bmatrix}. \tag{19}$$

The coefficient matrix $\boldsymbol{C}_2$ of the first scheme yields a second-order accurate solution on equidistant grids. A fourth-order integration scheme is obtained with $\boldsymbol{C}_4$. Preliminary tests showed that the difference between these operators has negligible effects on the computed energy and dissipation spectra. Therefore, we use the simple second-order integration $\boldsymbol{C}_2$ throughout this paper.

A remark on the discretization of the Poisson equation (4) is in order. Langford and Moser [20] have pointed out that, given a divergence-free continuous turbulence field, for the corresponding filtered field a divergence residual arises. They propose to adjust the discrete divergence operator appropriately. A similar issue is faced with ALDM where an adaptive reconstruction could also be used for the discrete divergence operator. However, in doing so the implicit model would become significantly more complex. Zandonade et al. [10] come to the conclusion that the accuracy gained by the adjusted discrete divergence operator does not justify the increased complexity and employ standard discrete operators. We follow this conclusion and employ a fourth-order finite-volume discretization of the Poisson equation (4). Parameters of ALDM, as will be shown below, enter the discrete Poisson equation by the discretization of the convective fluxes. Since energy redistribution due to pressure thus also contains the adaptive deconvolution through the discrete divergence of the convective fluxes the model parameters which will be determined in Section 3.3 reflect both contributions to the energy transfer.

2.2. Solution-adaptive local deconvolution and interpolation

As a consequence of identity (16), finite-volume schemes require a reconstruction of data at the faces of the computational volumes which corresponds to approximate deconvolution [13]. The 3D filter operation is defined in Eq. (1). The 3D top-hat filter kernel can be factorized into three 1D operators

$$\boldsymbol{G}(\boldsymbol{x}) = \boldsymbol{G}_x(x) * \boldsymbol{G}_y(y) * \boldsymbol{G}_z(z). \tag{20}$$

An inverse-filter operation can be defined as a convolution with the inverse kernel

$$\boldsymbol{G}^{-1}(\boldsymbol{x}) = \boldsymbol{G}_x^{-1}(x) * \boldsymbol{G}_y^{-1}(y) * \boldsymbol{G}_z^{-1}(z), \tag{21}$$

factorized into three 1D operators. An exact inverse filter operation is ill-posed and a de-filtered solution can only be computed approximately by regularized deconvolution [6]. Therefore, we first modify and extend the reconstruction (i.e., deconvolution and interpolation) operator of 1D ALDM from [13] appropriately. This operator, denoted by χ_x^λ, is defined on a 1D grid $x_N = \{x_i\}$. Applied to the filtered grid function $\bar{\varphi}_N = \{\bar{\varphi}(x_i)\}$ it returns the approximately deconvolved grid function $\widetilde{\varphi}_N^\lambda \doteq \{\varphi(x_{i+\lambda})\}$ on the shifted grid $x_N^\lambda = \{x_{i+\lambda}\}$

$$\chi_x^\lambda \bar{\varphi}_N = \left\{\varphi(\widetilde{\varphi}, x_{i+\lambda}) + \mathcal{O}\left(\Delta x_i^\kappa\right)\right\} = \widetilde{\varphi}_N^\lambda. \tag{22}$$

The filtered data are given at the cell centers $\{x_i\}$. Reconstruction at the left cell faces $\{x_{i-\frac{1}{2}}\}$ is indicated by $\lambda = -1/2$ and at the right faces by $\lambda = +1/2$. For obtaining a 3D reconstruction by successive 1D operations yet another approximation of the partially deconvolved solution is required at the cell centers. The respective operator is indicated by $\lambda = 0$.

Deconvolution and interpolation are done simultaneously using Lagrangian interpolation polynomials as proposed by Harten et al. [21]. Given a generic k-point stencil ranging from x_{i-r} to $x_{i-r+k-1}$ the 1D ansatz for the top-hat kernel (11) reads

$$\varphi(x_{i+\lambda}) = \sum_{l=0}^{k-1} c_{k,r,l}^\lambda(x_i)\bar{\varphi}_N(x_{i-r+l}) + \mathcal{O}\left(\Delta x_i^k\right) \tag{23}$$

with $r \in \{0,\ldots,k\}$. The grid-dependent coefficients are

$$c_{k,r,l}^\lambda(x_i) = \left(x_{i-r+l+\frac{1}{2}} - x_{i-r+l-\frac{1}{2}}\right) \sum_{m=l+1}^{k} \frac{\sum_{\substack{p=0\\p\neq m}}^{k} \prod_{\substack{n=0\\n\neq p,m}}^{k} x_{i+\lambda} - x_{i-r+n-\frac{1}{2}}}{\prod_{\substack{n=0\\n\neq m}}^{k} x_{j-r+m-\frac{1}{2}} - x_{i-r+n-\frac{1}{2}}}, \tag{24}$$

as given by Shu [22], and apply for grids with variable mesh width and for arbitrary target positions $x_{i+\lambda}$. In case of a staggered grid the values of x_i are different for each velocity component and the coefficients $c_{k,r,l}^\lambda$ have to be specified accordingly.

Selecting a particular interpolation stencil would return a linear discretization with a fixed, solution independent functional expression of the kth order truncation error, provided the function is sufficiently smooth on the interpolation stencil. ALDM adopts the idea of the weighted-essentially-non-oscillatory (WENO) scheme of Shu [22] where interpolation polynomials of a single order $k \equiv K$ are selected and combined non-linearly. The essential difference between ALDM and WENO is that we superpose all interpolants of order $k = 1,\ldots,K$

$$\widetilde{\varphi}_N^\lambda(x_{i+\lambda}) = \sum_{k=1}^{K} \sum_{r=0}^{k-1} \omega_{k,r}^\lambda(\bar{\varphi}_N, x_i) \sum_{l=0}^{k-1} c_{k,r,l}^\lambda(x_i)\bar{\varphi}_N(x_{i-r+l}) \tag{25}$$

to allow for lower-order contributions to the truncation error for implicit SGS modeling [13]. The weights $\omega_{k,r}^\lambda(\bar{\varphi}_N, x_i)$ can be constructed as to yield an accurate approximation of order $\kappa = 2K-1$ in smooth regions [22]. For our purpose, however, we do not need highest possible order of accuracy. Rather the superposition (25) introduces free discretization parameters which allow to control error cancellations. The sum of all weights is constrained to be unity for consistency. More restrictively we require

$$\sum_{r=0}^{k-1} \omega_{k,r}^\lambda = \frac{1}{K} \tag{26}$$

with $k = 1,\ldots,K$, and compute each weight from

$$\omega_{k,r}^\lambda(\bar{\varphi}_N, x_i) = \frac{1}{K} \frac{\gamma_{k,r}^\lambda \beta_{k,r}(\bar{\varphi}_N, x_i)}{\sum_{s=0}^{k-1} \gamma_{k,s}^\lambda \beta_{k,s}(\bar{\varphi}_N, x_i)} \tag{27}$$

with $r = 0,\ldots,k-1$ for each $k = 1,\ldots,K$. The solution-adaptive behavior of ALDM is controlled by the functional

$$\beta_{k,r}(\bar{\varphi}_N, x_i) = \left(\varepsilon_\beta + \sum_{l=-r}^{k-r-2} \left(\bar{\varphi}_{i+m+1} - \bar{\varphi}_{i+m} \right)^2 \right)^{-2}, \tag{28}$$

where ε_β is a small number to prevent division by zero. $\beta_{k,r}$ measure the smoothness of the grid function on the respective stencil to obtain a nonlinear adaptation of the deconvolution. Alternative smoothness measures for WENO schemes have been proposed by Liu et al. [23] and by Jiang and Shu [24].

The parameters $\gamma_{k,r}^{+1/2}$, $\gamma_{k,r}^{-1/2}$, and $\gamma_{k,r}^{0}$ represent a stencil-selection preference that would become effective in the statistically homogeneous case. The requirement of an isotropic discretization for this case implies symmetries on the parameters

$$\gamma_{k,r}^{-1/2} = \gamma_{k,k-1-r}^{+1/2} \quad \text{and} \quad \gamma_{k,r}^{0} = \gamma_{k,k-1-r}^{0}. \tag{29}$$

As consequence of Eq. (26) the number of independent parameters is further reduced by

$$\sum_{r=0}^{k-1} \gamma_{k,r}^{+1/2} = 1 \quad \text{and} \quad \sum_{r=0}^{k-1} \gamma_{k,r}^{0} = 1. \tag{30}$$

In the present implementation of ALDM we use $K = 3$. Hence, four parameters $\{\gamma_{2,0}^{+1/2}, \gamma_{3,0}^{+1/2}, \gamma_{3,1}^{+1/2}, \gamma_{3,1}^{0}\}$ are available for modeling.

We assemble now the 3D adaptive local deconvolution operator $\boldsymbol{\chi}^{\boldsymbol{\lambda}}$ from 1D operators of the kind of χ_x^{λ}. Following Eq. (21) we obtain

$$\widetilde{\bar{\varphi}}_N^{\boldsymbol{\lambda}} = \boldsymbol{\chi}^{\boldsymbol{\lambda}} \bar{\varphi}_N = \chi_z^{\lambda_3}(\chi_y^{\lambda_2}(\chi_x^{\lambda_1} \bar{\varphi}_N)). \tag{31}$$

Analogous to the procedure in 1D the vector $\boldsymbol{\lambda} = [\lambda_1,\lambda_2,\lambda_3]$ indicates the relative target position. Required operations are summarized in Table 1. Theoretically, the sequence of these 1D operators is arbitrary. However, there is a certain preferred choice which minimizes computational cost. Since each operator in Table 1 consists of two centered and one shift step, operations with $\lambda = \pm 1/2$ should be performed last. Furthermore, the order should be chosen by cyclic permutation to achieve rotational invariance of the implicit model. For example, to compute the approximately deconvolved solution $\widetilde{\boldsymbol{u}}_{ijk}^{\mathrm{L}}$ at the left cell face $\boldsymbol{\lambda} = [-1/2,0,0]$ we first perform a 1D deconvolution in y-direction using the central operator χ_y^0. Then, another 1D operator χ_z^0 is applied to the partially deconvolved solution. Only in the final step the deconvolved solution is interpolated to the target position by $\chi_x^{-1/2}$. For computational efficiency, we simultaneously compute $\widetilde{\boldsymbol{u}}_{ijk}^{\mathrm{R}}$ by applying $\chi_x^{+1/2}$ in the final step. Note that $\widetilde{\boldsymbol{u}}_{i-1jk}^{\mathrm{R}}$ stands for a second approximation at the same cell face as $\widetilde{\boldsymbol{u}}_{ijk}^{\mathrm{L}}$ but with the neighbor cell I_{i-1jk} as reference (see Table 2).

2.3. Numerical flux function

Once the reconstruction of the velocity solution at the cell faces is known, the numerical flux $\widetilde{\boldsymbol{F}}_N = [{}^1\widetilde{\boldsymbol{f}}, {}^2\widetilde{\boldsymbol{f}}, {}^3\widetilde{\boldsymbol{f}}]$ can be computed. A consistent numerical flux function approximates the physical flux function

$$\widetilde{\boldsymbol{F}}_N \approx \boldsymbol{F} = \boldsymbol{u}\boldsymbol{u} \quad \text{and} \quad {}^l\widetilde{\boldsymbol{f}} \approx {}^l\boldsymbol{f} = u_l \boldsymbol{u}. \tag{32}$$

Table 1
Interpolation directions for 3D reconstruction

Direction	Relative target index λ	Example
(R) rightward	$[+\frac{1}{2},0,0]$	$\widetilde{\boldsymbol{u}}_{i,j,k}^{\mathrm{R}} \approx \boldsymbol{u}(x_{i+\frac{1}{2}}, y_j, z_k)$
(L) leftward	$[-\frac{1}{2},0,0]$	$\widetilde{\boldsymbol{u}}_{i,j,k}^{\mathrm{L}} \approx \boldsymbol{u}(x_{i-\frac{1}{2}}, y_j, z_k)$
(F) forward	$[0,+\frac{1}{2},0]$	$\widetilde{\boldsymbol{u}}_{i,j,k}^{\mathrm{F}} \approx \boldsymbol{u}(x_i, y_{j+\frac{1}{2}}, z_k)$
(B) backward	$[0,-\frac{1}{2},0]$	$\widetilde{\boldsymbol{u}}_{i,j,k}^{\mathrm{B}} \approx \boldsymbol{u}(x_i, y_{j-\frac{1}{2}}, z_k)$
(U) upward	$[0,0,+\frac{1}{2}]$	$\widetilde{\boldsymbol{u}}_{i,j,k}^{\mathrm{U}} \approx \boldsymbol{u}(x_i, y_j, z_{k+\frac{1}{2}})$
(D) downward	$[0,0,-\frac{1}{2}]$	$\widetilde{\boldsymbol{u}}_{i,j,k}^{\mathrm{D}} \approx \boldsymbol{u}(x_i, y_j, z_{k-\frac{1}{2}})$

Table 2
Result obtained by evolutionary optimization for the discretization parameters of ALDM

Parameter	Optimal value
$\mathscr{C}$	0.0054850
$\gamma_{3,1}^{0}$	0.0500300
$\gamma_{2,0}^{+1/2}$	1.0000000
$\gamma_{3,0}^{+1/2}$	0.0190200
$\gamma_{3,1}^{+1/2}$	0.0855000
σ	0.0689100

A review of common numerical flux functions can be found, e.g. in LeVeque's textbook [25]. During construction of the one-dimensional ALDM scheme various flux functions were analyzed by MDEA [13]. Based on these findings, we propose the following modification of a Lax–Friedrichs flux function:

$$ {}^{1}\tilde{\boldsymbol{f}}_{i+\frac{1}{2},j,k} = \frac{1}{4}\left(\widetilde{u}^{\mathrm{L}}_{i+1,j,k} + \widetilde{u}^{\mathrm{R}}_{i,j,k}\right)\left(\widetilde{\boldsymbol{u}}^{\mathrm{L}}_{i+1,j,k} + \widetilde{\boldsymbol{u}}^{\mathrm{R}}_{i,j,k}\right) - {}^{1}\sigma_{i,j,k}\begin{bmatrix} |\bar{u}_{i+1,j,k} - \bar{u}_{i,j,k}|(\widetilde{u}^{\mathrm{L}}_{i+1,j,k} - \widetilde{u}^{\mathrm{R}}_{i,j,k}) \\ |\bar{v}_{i+1,j,k} - \bar{v}_{i,j,k}|(\widetilde{v}^{\mathrm{L}}_{i+1,j,k} - \widetilde{v}^{\mathrm{R}}_{i,j,k}) \\ |\bar{w}_{i+1,j,k} - \bar{w}_{i,j,k}|(\widetilde{w}^{\mathrm{L}}_{i+1,j,k} - \widetilde{w}^{\mathrm{R}}_{i,j,k}) \end{bmatrix}, \tag{33a} $$

$$ {}^{2}\tilde{\boldsymbol{f}}_{i,j+\frac{1}{2},k} = \frac{1}{4}(\widetilde{v}^{\mathrm{B}}_{i,j+1,k} + \widetilde{v}^{\mathrm{F}}_{i,j,k})(\widetilde{\boldsymbol{u}}^{\mathrm{B}}_{i,j+1,k} + \widetilde{\boldsymbol{u}}^{\mathrm{F}}_{i,j,k}) - {}^{2}\sigma_{i,j,k}\begin{bmatrix} |\bar{u}_{i,j+1,k} - \bar{u}_{i,j,k}|(\widetilde{u}^{\mathrm{B}}_{i,j+1,k} - \widetilde{u}^{\mathrm{F}}_{i,j,k}) \\ |\bar{v}_{i,j+1,k} - \bar{v}_{i,j,k}|(\widetilde{v}^{\mathrm{B}}_{i,j+1,k} - \widetilde{v}^{\mathrm{F}}_{i,j,k}) \\ |\bar{w}_{i,j+1,k} - \bar{w}_{i,j,k}|(\widetilde{w}^{\mathrm{B}}_{i,j+1,k} - \widetilde{w}^{\mathrm{F}}_{i,j,k}) \end{bmatrix}, \tag{33b} $$

$$ {}^{3}\tilde{\boldsymbol{f}}_{i,j,k+\frac{1}{2}} = \frac{1}{4}(\widetilde{w}^{\mathrm{D}}_{i,j,k+1} + \widetilde{w}^{\mathrm{U}}_{i,j,k})(\widetilde{\boldsymbol{u}}^{\mathrm{D}}_{i,j,k+1} + \widetilde{\boldsymbol{u}}^{\mathrm{U}}_{i,j,k}) - {}^{3}\sigma_{i,j,k}\begin{bmatrix} |\bar{u}_{i,j,k+1} - \bar{u}_{i,j,k}|(\widetilde{u}^{\mathrm{D}}_{i,j,k+1} - \widetilde{u}^{\mathrm{U}}_{i,j,k}) \\ |\bar{v}_{i,j,k+1} - \bar{v}_{i,j,k}|(\widetilde{v}^{\mathrm{D}}_{i,j,k+1} - \widetilde{v}^{\mathrm{U}}_{i,j,k}) \\ |\bar{w}_{i,j,k+1} - \bar{w}_{i,j,k}|(\widetilde{w}^{\mathrm{D}}_{i,j,k+1} - \widetilde{w}^{\mathrm{U}}_{i,j,k}) \end{bmatrix} \tag{33c} $$

for the three-dimensional Navier–Stokes equations and collocated grids.

The first term on the right-hand side corresponds to the physical Navier–Stokes flux. For maximum order of consistency, it is computed from the mean of both interpolants of the deconvolved velocity at the considered cell face. The difference between them is exploited as an estimate of the local truncation error. In the second term on the right-hand side, it is multiplied with the magnitude of a filtered velocity increment which corresponds to the first-order structure function. For developed turbulence the Kolmogorov theory predicts a scaling with a 1/3 power of the two-point separation [26]. We found that the compensation coefficients:

$$ {}^{1}\sigma_{i,j,k} = \sigma\left(\frac{x_{i+1,j,k} - x_{i,j,k}}{\Delta_0}\right)^{-\frac{1}{3}}, \tag{34a} $$

$$ {}^{2}\sigma_{i,j,k} = \sigma\left(\frac{y_{i,j+1,k} - y_{i,j,k}}{\Delta_0}\right)^{-\frac{1}{3}}, \tag{34b} $$

$$ {}^{3}\sigma_{i,j,k} = \sigma\left(\frac{z_{i,j,k+1} - z_{i,j,k}}{\Delta_0}\right)^{-\frac{1}{3}}, \tag{34c} $$

ensure a resolution independent numerical viscosity, see Section 3.2, as long as the numerical cutoff is located within the inertial range of the kinetic-energy spectrum. As consequence of the optimum-value determination procedure in Section 3.3 the reference length scale is $\Delta_0 = 2\pi/32$. The scalar factor σ adds another free parameter to ALDM. It is interesting to note that with this kind of grid-width compensation the truncation error of ALDM, when formally determined by Taylor series expansion, is less than second order in terms of the mesh width.

3. Subgrid-scale modeling

3.1. Modified-differential-equation analysis in real space

By an analysis of the modified differential equation (8) an implicit SGS model can be determined analytically. It can be observed that the truncation error of nonlinear discretization schemes contains functional expressions which are similar to explicit SGS models [27,28]. By adjusting the truncation error appropriately a match between an implicit and an explicit SGS model can be obtained [13].

For clarity it is common to restrict the analysis of the MDE to the top-hat filter and a uniform grid size. Consistent with the spatial-filtering approach the time step is assumed to be sufficiently small so that all relevant time scales are well resolved. The truncation error $\mathscr{G}_N$ is given by

$$\mathscr{G}_N = \boldsymbol{G} * \boldsymbol{\nabla} \cdot \boldsymbol{N}_N(\boldsymbol{u}_N) - \widetilde{\boldsymbol{G}} * \widetilde{\boldsymbol{\nabla}} \cdot \widetilde{\boldsymbol{N}}_N(\widetilde{\boldsymbol{u}}_N) = \{\boldsymbol{G} * \boldsymbol{\nabla} \cdot \boldsymbol{u}_N \boldsymbol{u}_N + \boldsymbol{\nabla} \bar{p}_N\} - \left\{\widetilde{\boldsymbol{G}} * \widetilde{\boldsymbol{\nabla}} \cdot \widetilde{\boldsymbol{F}}_N(\widetilde{\boldsymbol{u}}_N) + \boldsymbol{\nabla} \tilde{p}_N\right\}. \tag{35}$$

For uniform viscosity and density the diffusive term is linear in terms of $\boldsymbol{u}_N$ and does not contribute to the SGS tensor. The pressure gradient is included in Eq. (35) since it is directly coupled to the convective term by the pressure-Poisson equation (4). The pressure gridfunction $\bar{p}_N$ corresponds to the filtered velocity field $\bar{\boldsymbol{u}}_N$ whereas the MDE solves for $\tilde{p}_N$. The residual $\tilde{\tilde{p}}_N = \tilde{p}_N - \bar{p}_N$ is the contribution of the pressure projection to the truncation error

$$\mathscr{G}_N = [\boldsymbol{G} * \boldsymbol{\nabla} \cdot \boldsymbol{u}_N \boldsymbol{u}_N - \widetilde{\boldsymbol{G}} * \widetilde{\boldsymbol{\nabla}} \cdot \widetilde{\boldsymbol{F}}_N(\widetilde{\boldsymbol{u}}_N)] - \boldsymbol{\nabla} \tilde{\tilde{p}}_N. \tag{36}$$

For an analytical expression of the first term on the right-hand side

$$\mathscr{A}_L(\bar{\boldsymbol{u}}) = \boldsymbol{G} * \boldsymbol{\nabla} \cdot \boldsymbol{u}_N \boldsymbol{u}_N - \widetilde{\boldsymbol{G}} * \widetilde{\boldsymbol{\nabla}} \cdot \widetilde{\boldsymbol{F}}_N(\widetilde{\boldsymbol{u}}_N) + \mathscr{O}(\Delta^L), \tag{37}$$

the filtered and the unfiltered solution are approximated by Taylor expansions of $\bar{\boldsymbol{u}}_N$ truncated at order L [13]. Moreover, the implicit SGS model (36) is divergence free if the pressure residual satisfies

$$\boldsymbol{\nabla} \cdot \boldsymbol{\nabla} \tilde{\tilde{p}}_N = \boldsymbol{\nabla} \cdot \mathscr{A}_L(\bar{\boldsymbol{u}}). \tag{38}$$

The detailed evaluation of $\mathscr{G}_N$ similarly as in [13], however, is practically impossible. One reason is the difficulty in solving Eq. (38) analytically, see, e.g. Batchelor [29, chapter 5]. Since already the analytical expression of $\mathscr{A}_L$ becomes extremely lengthy the 3D problem is not tractable any longer even with symbolic-mathematics software.

3.2. Modified-differential-equation analysis in spectral space

In the following, we analyze the MDE in Fourier space in order to develop a theoretical framework for the evaluation of subgrid dissipation and spectral numerical viscosity of ALDM.

We consider the discretization of a $2\pi^3$-periodic domain. N is the number of grid points in one dimension and $\xi_C = N/2 - 1$ is the corresponding cut-off wave number in discrete Fourier space. Reference to spectral theories of turbulence implies isotropy. A physical-space discretization restricts contributions to the numerical solution to wavenumbers up to $|\boldsymbol{\xi}| = \sqrt{3}\xi_C$. For consistency with isotropy wave numbers with $|\boldsymbol{\xi}| > \xi_C$ need to be removed. For this purpose we define

$$\widehat{\boldsymbol{u}}_C(\boldsymbol{\xi}) = \begin{cases} \widehat{\boldsymbol{u}}_N(\boldsymbol{\xi}), & |\boldsymbol{\xi}| \leqslant \xi_C, \\ \boldsymbol{0}, & \text{otherwise}, \end{cases} \tag{39}$$

where the hat denotes the Fourier transform. The corresponding MDE in spectral space is:

$$\frac{\partial \widehat{\boldsymbol{u}}_C}{\partial t} + \widehat{\boldsymbol{G}} \mathrm{i}\boldsymbol{\xi} \cdot \widehat{\boldsymbol{N}}_C(\widehat{\boldsymbol{u}}_C) + \nu \boldsymbol{\xi}^2 \widehat{\boldsymbol{u}}_C = \widehat{\mathscr{G}}_C, \tag{40a}$$

$$\mathrm{i}\boldsymbol{\xi} \cdot \widehat{\boldsymbol{u}}_C = 0, \tag{40b}$$

where i is the imaginary unit and $\boldsymbol{\xi}$ is the wave-number vector. On the represented wave-number range the kinetic energy of the deconvolved velocity

$$\widehat{\boldsymbol{u}}_{\mathrm{C}}(\boldsymbol{\xi}) = \widehat{\boldsymbol{G}}^{-1}(\boldsymbol{\xi})\widehat{\bar{\boldsymbol{u}}}_{\mathrm{C}}(\boldsymbol{\xi}), \quad \text{with } |\boldsymbol{\xi}| \leqslant \xi_{\mathrm{C}} \tag{41}$$

is

$$\widehat{E}(\boldsymbol{\xi}) = \frac{1}{2}\widehat{\boldsymbol{u}}_{\mathrm{C}}(\boldsymbol{\xi}) \cdot \widehat{\boldsymbol{u}}^{*}_{\mathrm{C}}(\boldsymbol{\xi}). \tag{42}$$

Multiplying Eq. (40a) by the complex-conjugate $\widehat{\boldsymbol{u}}^{*}_{\mathrm{C}}$ of $\widehat{\boldsymbol{u}}_{\mathrm{C}}$ we obtain

$$\widehat{\boldsymbol{G}}\frac{\partial \widehat{E}(\boldsymbol{\xi})}{\partial t} - \widehat{\boldsymbol{G}}(\boldsymbol{\xi})\widehat{T}_{\mathrm{C}}(\boldsymbol{\xi}) + 2\nu\boldsymbol{\xi}^2\widehat{\boldsymbol{G}}\widehat{E}(\boldsymbol{\xi}) = \widehat{\boldsymbol{u}}^{*}_{\mathrm{C}}(\boldsymbol{\xi}) \cdot \widehat{\mathscr{G}}_{\mathrm{C}}(\boldsymbol{\xi}). \tag{43}$$

The nonlinear energy transfer

$$\widehat{T}_{\mathrm{C}}(\boldsymbol{\xi}) = \mathrm{i}\ \widehat{\boldsymbol{u}}^{*}_{\mathrm{C}} \cdot \boldsymbol{\xi} \cdot \widehat{\boldsymbol{N}}_{\mathrm{C}}(\widehat{\boldsymbol{u}}_{\mathrm{C}}) = \mathrm{i}\ \widehat{\boldsymbol{u}}^{*}_{\mathrm{C}}(\boldsymbol{\xi}) \cdot \boldsymbol{P}^3(\boldsymbol{\xi}) \cdot \int_{|\boldsymbol{\eta}| \leqq \xi_{\mathrm{C}}} \widehat{\boldsymbol{u}}_{\mathrm{C}}(\boldsymbol{\xi})\widehat{\boldsymbol{u}}_{\mathrm{C}}(\boldsymbol{\xi} - \boldsymbol{\eta})\,\mathrm{d}\boldsymbol{\eta} \tag{44}$$

is the Fourier transform of the nonlinear term. The tensor $\boldsymbol{P}^3(\boldsymbol{\xi})$ is defined by $\underset{lmn}{P^3}(\boldsymbol{\xi}) = \xi_m\delta_{\mathrm{ln}} - \xi_l\xi_m\xi_n|\boldsymbol{\xi}|^{-2}$, see also [30]. Finally, we deconvolve Eq. (43) by multiplication with the inverse filter coefficient $\widehat{G}^{-1}(\boldsymbol{\xi})$ which is defined on the range of represented scales $|\boldsymbol{\xi}| \leqq \xi_{\mathrm{C}}$ and obtain

$$\frac{\partial \widehat{E}(\boldsymbol{\xi})}{\partial t} - \widehat{T}_{\mathrm{C}}(\boldsymbol{\xi}) + 2\nu\boldsymbol{\xi}^2\widehat{E}(\boldsymbol{\xi}) = \widehat{\boldsymbol{G}}^{-1}(\boldsymbol{\xi})\widehat{\boldsymbol{u}}^{*}_{\mathrm{C}}(\boldsymbol{\xi}) \cdot \widehat{\mathscr{G}}_{\mathrm{C}}(\boldsymbol{\xi}). \tag{45}$$

The right-hand side of this equation is the numerical dissipation

$$\varepsilon_{\mathrm{num}}(\boldsymbol{\xi}) = -\widehat{\boldsymbol{G}}^{-1}(\boldsymbol{\xi})\widehat{\boldsymbol{u}}^{*}_{\mathrm{C}}(\boldsymbol{\xi}) \cdot \widehat{\mathscr{G}}_{\mathrm{C}}(\boldsymbol{\xi}) \tag{46}$$

implied by the discretization of the convective term. Now we investigate how to model the physical subgrid dissipation $\varepsilon_{\mathrm{SGS}}(\boldsymbol{\xi})$ by $\varepsilon_{\mathrm{num}}(\boldsymbol{\xi})$.

An exact analytical match between $\varepsilon_{\mathrm{num}}(\boldsymbol{\xi})$ and $\varepsilon_{\mathrm{SGS}}(\boldsymbol{\xi})$ cannot be achieved since $\varepsilon_{\mathrm{SGS}}(\boldsymbol{\xi})$ involves interactions with non-represented scales. Modeling can be accomplished by invoking theoretical energy-transfer expressions. Employing an eddy-viscosity hypothesis the subgrid-scale dissipation is

$$\varepsilon_{\mathrm{SGS}}(\boldsymbol{\xi}) = 2\nu_{\mathrm{SGS}}(\boldsymbol{\xi})\xi^2\widehat{E}(\boldsymbol{\xi}). \tag{47}$$

Similarly, the numerical dissipation can be expressed as

$$\nu_{\mathrm{num}}(\boldsymbol{\xi}) = \frac{\varepsilon_{\mathrm{num}}(\boldsymbol{\xi})}{2\xi^2\widehat{E}(\boldsymbol{\xi})}. \tag{48}$$

In general ν_{num} is a function of the wavenumber vector $\boldsymbol{\xi}$. For isotropic turbulence, however, statistical properties of Eq. (45) follow from the scalar evolution equation for the 3D energy spectrum

$$\frac{\partial \widehat{E}(\xi)}{\partial t} - \widehat{T}_{\mathrm{C}}(\xi) + 2\nu\xi^2\widehat{E}(\xi) = -\varepsilon_{\mathrm{num}}(\xi). \tag{49}$$

This equation is obtained from Eq. (45) by integration over spherical shells with radius $\xi = |\boldsymbol{\xi}|$

$$\widehat{\varphi}(\xi) = \oint_{|\boldsymbol{\xi}|=\xi} \hat{\varphi}(\boldsymbol{\xi})\,\mathrm{d}\boldsymbol{\xi}. \tag{50}$$

For a given numerical scheme $\nu_{\mathrm{num}}(\xi)$ can be computed from

$$\nu_{\mathrm{num}}(\xi) = -\frac{\widehat{G}^{-1}(\xi)}{2\xi^2\widehat{E}(\xi)} \int_{|\boldsymbol{\xi}|=\xi} \widehat{\boldsymbol{u}}^{*}_{N}(\boldsymbol{\xi}) \cdot \widehat{\mathscr{G}}_{N}(\boldsymbol{\xi})\,\mathrm{d}\boldsymbol{\xi}. \tag{51}$$

Convenient for our purposes is a normalization by

$$\nu^{+}_{\mathrm{num}}(\xi^{+}) = \nu_{\mathrm{num}}\left(\frac{\xi}{\xi_{\mathrm{C}}}\right)\sqrt{\frac{\xi_{\mathrm{C}}}{\widehat{E}(\xi_{\mathrm{C}})}}, \tag{52}$$

with $\xi^+ = \frac{\xi}{\xi_C}$ as proposed by Chollet and Lesieur [31]. The concept of a wavenumber-dependent spectral eddy viscosity was first proposed by Heisenberg [32].

For high Reynolds numbers and under the assumption of a Kolmogorov range $E(\xi) = C_K \varepsilon^{3/2} \xi^{-5/3}$ extending to infinity the Eddy-Damped Quasi-Normal Markovian (EDQNM) theory [8] leads to

$$\nu^+_{SGS}(\xi^+) = 0.441 C_K^{-3/2} X(\xi^+), \tag{53}$$

where C_K is the Kolmogorov constant and $X(\xi^+)$ is a non-dimensional function exhibiting a plateau at unity for small wavenumbers $\xi^+ \lesssim 1/3$ and a sharply rising cusp in the vicinity of the cut-off wave number $\xi^+ = 1$. Chollet [17] proposes the expression

$$\nu^+_{Chollet}(\xi^+) = 0.441 C_K^{-3/2} (1 + 34.467 e^{-3.03/\xi^+}) \tag{54}$$

as best fit to the exact solution.

3.3. Numerical evaluation and optimization of the numerical viscosity

We consider freely decaying homogeneous isotropic turbulence in the limit of vanishing molecular viscosity. A numerical simulation is performed in a $(2\pi)^3$-periodic box, discretized by $32 \times 32 \times 32$ uniform finite volumes. Filtered and truncated LES data obtained with a dynamic Smagorinsky model at higher spatial resolution are used as initial condition $\bar{\boldsymbol{u}}_N(t_0)$. Solutions $\bar{\boldsymbol{u}}_N(t_n)$ at time $t_n = t_0 + n\Delta t$, n being an integer, are obtained by advancing n time steps with ALDM. An a posteriori analysis of the data allows to identify the spectral eddy viscosity of the implicit SGS model. For this purpose, an algorithm proposed by Domaradzki et al. [18] is adapted.

The computed velocity fields $\bar{\boldsymbol{u}}_N(t_n)$ are Fourier-transformed and truncated at $\xi_C = 15$

$$\widehat{\bar{\boldsymbol{u}}}_C(\boldsymbol{\xi}, t_n) = \begin{cases} \mathscr{F}\{\bar{\boldsymbol{u}}_N\}(\boldsymbol{\xi}, t_n), & |\boldsymbol{\xi}| \leqslant \xi_C, \\ \boldsymbol{0}, & \text{otherwise.} \end{cases} \tag{55}$$

Energy spectra $\widehat{E}(\boldsymbol{\xi}, t_n)$ and spectral transfer functions $\widehat{T}_C(\boldsymbol{\xi}, t_n)$ are computed from Eqs. (42) and (44). The convolution integral in Eq. (44) is computed in real space. The computation of the numerical-dissipation spectrum, Eqs. (45) and (46), involves the spectral-energy decay which is approximated by

$$\frac{\partial \widehat{E}(\boldsymbol{\xi}, t_{n-1/2})}{\partial t} \approx \frac{\widehat{E}(\boldsymbol{\xi}, t_n) - \widehat{E}(\boldsymbol{\xi}, t_{n-1})}{\Delta t} \tag{56}$$

at times $t_{n-1/2} = \frac{1}{2}(t_{n-1} + t_n)$. Energy spectrum and spectral transfer function are interpolated as:

$$\widehat{E}(\boldsymbol{\xi}, t_{n-1/2}) = \frac{\widehat{E}(\boldsymbol{\xi}, t_n) + \widehat{E}(\boldsymbol{\xi}, t_{n-1})}{2}, \tag{57a}$$

$$\widehat{T}_C(\boldsymbol{\xi}, t_{n-1/2}) = \frac{\widehat{T}_C(\boldsymbol{\xi}, t_n) + \widehat{T}_C(\boldsymbol{\xi}, t_{n-1})}{2}. \tag{57b}$$

Following Eq. (48) the spectral numerical viscosity is

$$\nu_{num}(\boldsymbol{\xi}, t_{n-1/2}) = \frac{1}{2\boldsymbol{\xi}^2 \widehat{E}(\boldsymbol{\xi}, t_{n-1/2})} \left(\widehat{T}_C(\boldsymbol{\xi}, t_{n-1/2}) - \frac{\partial \widehat{E}(\boldsymbol{\xi}, t_{n-1/2})}{\partial t} \right) - \nu. \tag{58}$$

The 3D numerical-viscosity spectrum is obtained by summation over integer-wavenumber shells $\xi - \frac{1}{2} \leqslant |\boldsymbol{\xi}| \leqslant \xi + \frac{1}{2}$

$$\nu_{num}(\xi, t_{n-1/2}) = \frac{4\pi\xi^2}{M(\xi)} \sum_{\boldsymbol{\xi}} \nu_{num}(\boldsymbol{\xi}, t_{n-1/2}), \tag{59}$$

where $M(\xi)$ is the number of integer wavenumbers on each shell with radius ξ. A subsequent normalization gives

$$v^{+}_{\mathrm{num}}(\xi^{+}, t_{n-1/2}) = \nu_{\mathrm{num}}(\xi_{\mathrm{C}}\xi^{+}, t_{n-1/2})\sqrt{\frac{\xi_{\mathrm{C}}}{\widehat{E}(\xi_{\mathrm{C}})}}. \tag{60}$$

Isotropic decaying turbulence does not lose memory of the initial data. An evaluation of v^{+}_{num} for one data set only does not necessarily represent the statistical average. To cope with this problem the spectral numerical viscosity from 10 uncorrelated realizations is evaluated and averaged. Each realization is advanced by one time step so that computational cost amounts to 10 time steps per evaluated numerical viscosity. Therefore, the evaluation procedure is sufficiently efficient for an automatic optimization of the free parameter values of the discretization scheme. As cost function $\mathscr{C}$, we define the root-mean-square difference between the spectral numerical viscosity $v^{+}_{\mathrm{num}}(\xi^{+})$ and the spectral eddy viscosity $v^{+}_{\mathrm{Chollet}}(\xi^{+})$ of EDQNM.

The employed automatic optimization algorithm [13,33] follows an evolutionary strategy and is particularly suitable for treating non-smooth cost functions. For completeness computational details of the optimization are summarized in Appendix A.

The finally selected optimal set of parameters is given in Table A.1. The spectral eddy viscosity of the ALDM scheme with the optimized parameter set yields an excellent match with theoretical predictions as shown in Fig. 1. It exhibits a low-wavenumber plateau at the correct level and reproduces the typical cusp shape up to the cut-off wave number at the correct magnitude.

ALDM nonlinearly combines interpolants from several central, upwind, and downwind stencils. The truncation error therefore is not purely dissipative. The probability density function (PDF) of the numerical viscosity $v^{+}_{\mathrm{num}}(\boldsymbol{\xi})$, shown in Fig. 2, exhibits significant anti-dissipative contributions which represent backscatter. Analysis of DNS data give a wide distribution of $v^{+}_{\mathrm{SGS}}(\boldsymbol{\xi})$ including negative values since the magnitude of local backscatter is comparable with and often even larger than the average subgrid energy transfer (e.g. [34]). The shell-averaged spectral eddy viscosity $v^{+}_{\mathrm{Chollet}}(\xi^{+})$ considers the net SGS dissipation only. Modeling backscatter renders a SGS model more realistic (e.g. [35,36]), whereas the particular way in which it is accounted for appears to be less important. An analysis of Carati et al. [37] revealed no major differences between the performance of stochastic and deterministic backscatter models.

4. Computational results

For a posteriori validation of the implicit SGS model provided by ALDM we perform LES of large-scale forced turbulence and of decaying isotropic turbulence. As an example for transitional flows we also consider the instability and breakdown of the 3D Taylor–Green vortex. All simulations presented in this section are carried out in a $(2\pi)^3$-periodic computational domain. The computational domain is discretized by 64^3 cells unless specified otherwise. For time advancement, we use an explicit third-order Runge–Kutta scheme of Shu [38,39]. The time step Δt is adjusted dynamically according to the Courant–Friedrichs–Lewy limit

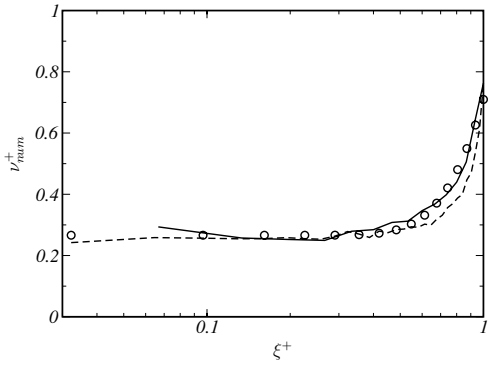

Fig. 1. Numerical viscosity of ALDM with optimized parameters compared to the prediction of turbulence theory. —— LES with $N = 32$, ---- LES with $N = 64$, ○ EDQNM theory [17].

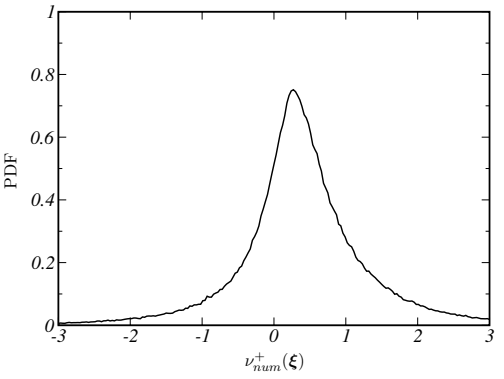

Fig. 2. PDF of normalized spectral numerical viscosity $\nu^+_{\mathrm{num}}(\xi)$ of ALDM with optimized parameters and with $N = 64$.

$$\Delta t = \mathrm{CFL}\min\left(\frac{\bar{u}_i}{\Delta x_i} + \frac{\nu}{\Delta x_i^2}\right)^{-1}, \tag{61}$$

where CFL is the Courant number. The time-discretization scheme is total-variation diminishing (TVD) for $\mathrm{CFL} \leqslant 1$, provided the underlying spatial discretization is TVD, whereas the linear stability bound is larger. Titarev and Toro [40] have observed that 3D finite-volume WENO schemes can be unstable for $\mathrm{CFL} > 1/3$. We found for ALDM stable time advancement up to the linear bound $\mathrm{CFL} = 1.7$. For all our simulations we use $\mathrm{CFL} = 1.0$.

ALDM applies only to the convective term of the NSE. The discretization schemes for dissipative terms and the pressure-Poisson equation are based on 4th-order Langrangian interpolation polynomials. First derivatives are approximated on 5-point central stencils

$$(\partial_x \bar{\varphi})_j = \frac{1}{\Delta x}\left[\frac{8}{12}(\bar{\varphi}_{j+1} - \bar{\varphi}_{j-1}) - \frac{1}{12}(\bar{\varphi}_{j+2} - \bar{\varphi}_{j-2})\right]. \tag{62}$$

In this paper we consider periodic domains only. Therefore, the Helmholtz projection of the velocity onto a divergence-free field is done in spectral space. For consistency with the underlying discretization scheme modified wavenumbers corresponding to Eq. (62) are used for solving the discrete Poisson equation.

4.1. Forced homogeneous isotropic turbulence

As first test case ALDM is applied to forced isotropic turbulence governed by:

$$\frac{\partial \bar{\boldsymbol{u}}_N}{\partial t} + \widetilde{G} * \widetilde{\boldsymbol{\nabla}} \cdot \widetilde{\boldsymbol{N}}_N(\widetilde{\boldsymbol{u}}_N) - \nu \boldsymbol{\nabla} \cdot \boldsymbol{\nabla} \bar{\boldsymbol{u}}_N = \boldsymbol{S}(\bar{\boldsymbol{u}}_N), \tag{63a}$$

$$\boldsymbol{\nabla} \cdot \bar{\boldsymbol{u}}_N = 0. \tag{63b}$$

The forcing $\boldsymbol{S}(\bar{\boldsymbol{u}}_N)$ is added to the right-hand side as an extra source term. It is defined in spectral space through its Fourier transform

$$\widehat{\boldsymbol{S}}(\boldsymbol{\xi}) = -C_{\mathrm{S}}(\xi)\widehat{\bar{\boldsymbol{u}}}(\boldsymbol{\xi}), \tag{64}$$

where $\xi = |\boldsymbol{\xi}|$. The forcing results in a production of kinetic energy that compensates dissipation while preserving the shape of the kinetic-energy spectrum. By construction of the linear compensation factor $C_{\mathrm{S}}(\xi)$ only large scales are affected by the forcing

$$C_{\mathrm{S}}(\xi) = \begin{cases} (2\widehat{E}'(\xi,t))^{-1}\dfrac{\partial \widehat{E}'(\xi,t)}{\partial t}, & \xi \leqslant \xi_{\mathrm{S}}, \\ 0, & \text{otherwise}, \end{cases} \tag{65}$$

where $\widehat{E}'$ is an intermediate energy spectrum obtained by first solving Eq. (63) with $\boldsymbol{S} = \boldsymbol{0}$ at the known time level. In this section, the threshold wavenumber is $\xi_{\mathrm{S}} = 4$.

We perform simulations for four different cases corresponding to the combination of two different grids with two different Reynolds numbers. The coarser grid is composed of $N^3 = 32^3$, the finer one of $N^3 = 64^3$ evenly spaced cells. The computational Reynolds numbers $Re = 1/\nu$ are $Re = 10^2$ and $Re = 10^5$. For the lower Reynolds number the Kolmogorov length scale is on the order of the mesh size $\Delta x = 2\pi/N$ for $N = 64$. The initial condition is a divergence-free velocity field with random phases and with a 3D energy spectrum $\widehat{E}(\xi) = \frac{1}{2}\xi^{-5/3}$. After an initial transient of 250 time steps, samples of the 3D energy spectra were collected until a converged mean spectrum was observed.

The resulting 3D energy spectra are shown in Fig. 3. For $Re = 10^2$ the largest resolved wave numbers are within the dissipative range. A comparison with DNS data show that the energy spectra computed with ALDM are also correct at low Reynolds numbers. A characteristic and grid independent observation is that the energy spectra level out in the immediate neighborhood of the cut-off wavenumber ξ_C. For $Re = 10^5$ the 3D mean energy spectra coincide for both mesh resolutions and follow the Kolmogorov law. This result verifies a posteriori the optimum parameter set which was based on the corresponding theoretical prediction.

Fig. 4 shows results obtained with a pseudo-spectral code, where Chollet's spectral eddy viscosity is added explicitly. We note an excellent agreement between the Chollet–Lesieur SGS model, ALDM, and the theoretical prediction $\widehat{E}(\xi) \sim \xi^{-5/3}$, and DNS data, respectively. For a dissipative-range spectrum EDQNM predicts, e.g. a considerably lower plateau value for ν^+_{SGS} (e.g. [41]) which has also been noticed in DNS analyses (e.g. [42]). On this account the performance of the unmodified Chollet–Lesieur SGS model at $Re = 10^2$ is remarkable. A possible explanation is that the low-wavenumber forcing immediately compensates an overestimated SGS dissipation.

For $Re = 10^2$ the isotropic Taylor micro scale λ_T can be approximated in terms of the resolved 3D energy spectrum [43]. The micro-scale Reynolds number is

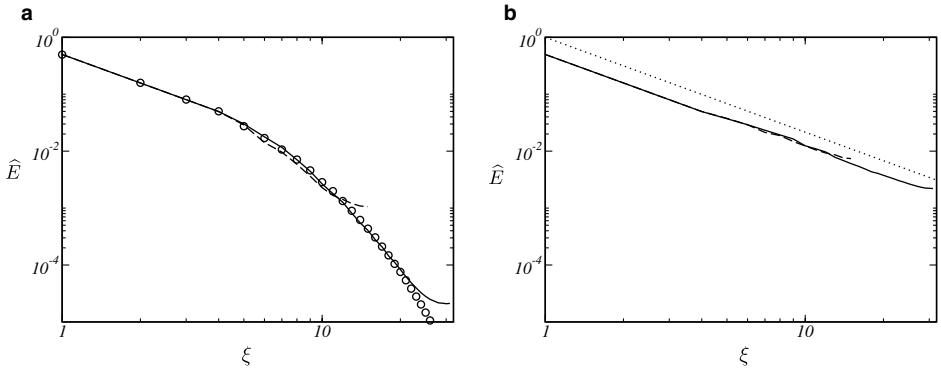

Fig. 3. Mean 3D energy spectra for the large-scale forced Navier–Stokes equation at (a) $Re = 100$, (b) $Re = 100000$; —— LES with 64^3 cells; ---- LES with 32^3 cells; ○ DNS; ····· line $\sim\xi^{-5/3}$.

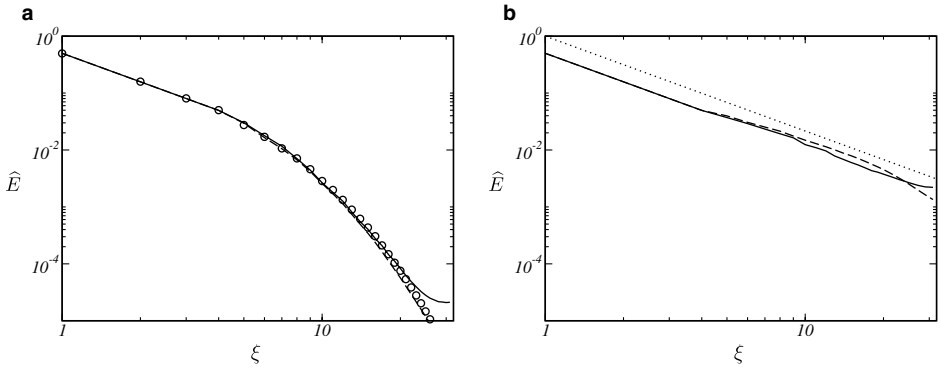

Fig. 4. Mean 3D energy spectra for LES of the large-scale forced Navier–Stokes equation at (a) $Re = 100$, (b) $Re = 100000$ with 64^3 cells; —— ALDM; ---- Chollet–Lesieur model; ○ DNS; ····· line $\sim\xi^{-5/3}$.

$$Re_\lambda = \frac{\lambda_T u'}{\nu} \tag{66}$$

with

$$\lambda_T \doteq \sqrt{\frac{5\sum_{\xi=1}^{\xi_C} \widehat{E}(\xi)}{\sum_{\xi=1}^{\xi_C} \xi^2 \widehat{E}(\xi)}}, \quad u' \doteq \sqrt{\frac{2}{3}\sum_{\xi=1}^{\xi_C} \widehat{E}(\xi)}. \tag{67}$$

The DNS predicts $Re_\lambda = 74$. Using ALDM we obtain $Re_\lambda = 78$ with $N = 32$ and $Re_\lambda = 73$ with $N = 64$. For the high-Re case λ_T cannot be computed by Eq. (67) since dissipative scales are not resolved. To quantify the SGS dissipation rate of ALDM at $Re \to \infty$ we consider freely decaying turbulence in the following section.

We conclude that with the model parameters found by an optimum match of a theoretical prediction for isotropic turbulence at $Re \to \infty$, see Section 3.3, the SGS dissipation predicted by ALDM correctly models the local energy transfer. This holds for cut-off wavenumbers ξ_C within the inertial range. The results also show that even for lower Reynolds numbers, for which ξ_C is in the dissipative range, the predicted spectral energy distribution and dissipation rate for the same parameter set are correct. This indicates that the used model parameters may be valid universally for isotropic turbulence. This is investigated in the following sections, where the parameter set is kept unchanged.

4.2. Decaying homogeneous isotropic turbulence at $Re \to \infty$

We integrate the Navier–Stokes equation by initially prescribing $\widehat{E}(\xi)$ as inertial-range spectrum for homogeneous isotropic turbulence in the limit $Re \to \infty$. After an initial transient during which the randomly oriented initial phases re-align by Navier–Stokes dynamics the energy spectrum decays self-similarly while preserving the $\xi^{-5/3}$ law up to the largest wavenumbers, see Fig. 5. This finding is consistent with LES results obtained with Chollet's eddy viscosity model available in the literature (e.g. [31,41,44]).

The observed decay rate $\varepsilon = -\partial K/\partial t$ of the resolved turbulent kinetic energy

$$K(t) = \sum_{1}^{\xi_C} \widehat{E}(\xi, t) \tag{68}$$

is proportional to the turbulent kinetic energy to the power of 3/2, see Fig. 6, as predicted by the scaling $\varepsilon \sim K^{3/2} l^{-1}$ for self-similar decay of an inertial-range spectrum, i.e., $l = \text{constant}$.

Decay rate and energy-spectrum shape can be assessed simultaneously by the Kolmogorov function

$$C_K(\xi, t) = \varepsilon(t)^{-2/3} \xi^{5/3} \widehat{E}(\xi, t), \tag{69}$$

which is plotted in Fig. 6. For an ideal setting the Kolmogorov function should be constant. For our simulations, we find a $C_K(\xi,t)$ which is almost constant in time and has a wide plateau in ξ at $C_K \approx 1.8$. This value

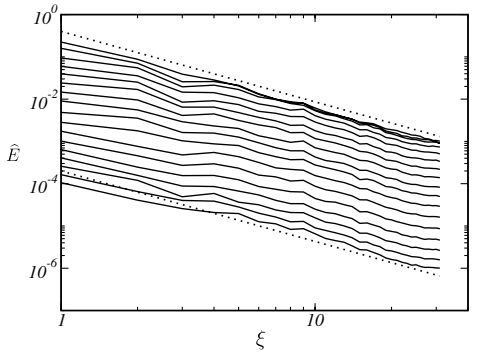

Fig. 5. Instantaneous 3D energy spectra for LES of decaying homogeneous isotropic turbulence at the inviscid limit. —— instantaneous spectra; ····· $\widehat{E} \sim \xi^{-5/3}$.

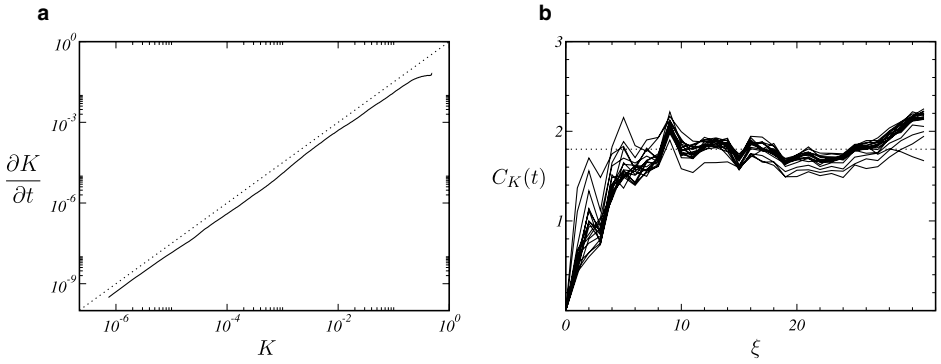

Fig. 6. (a) Phase diagram of turbulent kinetic energy and (b) Kolmogorov function for decaying homogeneous isotropic turbulence at $Re \to \infty$. ····· $\varepsilon \sim K^{3/2}$, $C_K = 1.8$, respectively.

slightly differs from theoretical predictions, but is in reasonable agreement with other published results. A comprehensive account of the value of the Kolmogorov constant in numerical simulations of isotropic turbulence is given by Yeung and Zhou [45].

4.3. Comte-Bellot–Corrsin experiment

A more complex situation is encountered for decaying grid-generated turbulence for which also the correct representation of the energy-containing range of the spectrum is important [30]. Computations are initialized with energy spectrum and Reynolds numbers adapted to the wind-tunnel experiments of Comte-Bellot and Corrsin [46], denoted hereafter as CBC.

Among other space-time correlations CBC provides streamwise energy spectra for grid-generated turbulence at three positions downstream of a mesh with a width $M = 5.08$ cm. Table 3 of [46] gives corresponding 3D energy spectra which were obtained under the assumption of isotropy. The grid Reynolds number of the experiment is $Re_M = 34000$, the Taylor-microscale Reynolds number is given as $Re_\lambda = 71.6$ at the first and $Re_\lambda = 60.6$ at the last position.

In the simulation, this flow is modeled as decaying turbulence in a $(2\pi)^3$-periodic computational domain. Based on the Taylor hypothesis the temporal evolution in the simulation corresponds to a downstream evolution in the wind-tunnel experiment with the experimental mean-flow speed which is approximately constant. The energy distribution of the initial velocity field is matched to the first measured 3D energy spectrum of CBC. The SGS model is verified by comparing computational and experimental 3D energy spectra at later time instants which correspond to the other two measuring stations.

The experimental data are non-dimensionalized as proposed in [47,48]. The reference velocity is $U_{\text{ref}} = \sqrt{3/2}\ 22.2$ cm/s, the reference length is $L_{\text{ref}} = 10.8M/2\pi$, and the reference time is $t_{\text{ref}} = L_{\text{ref}}/U_{\text{ref}}$. In order to create the initial velocity field a random field was allowed to develop for about one large-eddy turnover time while maintaining the 3D energy spectrum (Eqs. (63)–(65) with $\xi_S = \sqrt{3}\xi_C$) as given for the first measuring station.

Results of ALDM are compared with those obtained with a 4th-order central discretization and an explicit Smagorinsky SGS model and with a pseudo-spectral code and an explicit Chollet–Lesieur model. The Smagorinsky model is used in its conventional and in its dynamic version. For the conventional model [49,50] the parameter is set to $C_S = 0.18$. Lilly [51] derived this value for sufficiently large Reynolds numbers and a sharp spectral cut off in the inertial range assuming $C_K \approx 1.4$. The dynamic algorithm was proposed by Germano et al. [52]. Here, C_S is computed according to Lilly [53] and an average over the entire flow field is taken.

Examining the computed energy spectra, Fig. 7, and dissipation spectra, Fig. 8, we note that ALDM performs just as well as the dynamic Smagorinsky SGS model. It should be noted that we use the dynamic Smagorinsky model as an example for state-of-the-art SGS models and as a benchmark for isotropic turbulence.

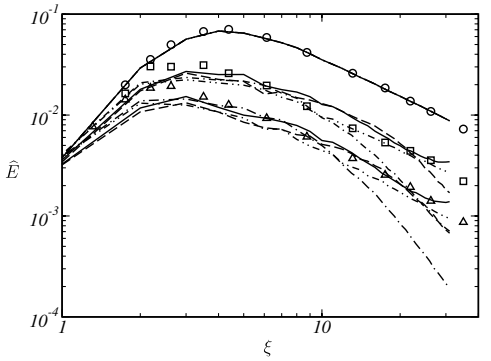

Fig. 7. Instantaneous 3D energy spectra for LES with 64^3 cells for the Comte-Bellot–Corrsin test case; ---- Chollet's eddy viscosity model, -·-·- Smagorinsky model, -···- dynamic Smagorinsky model, —— ALDM; ○ $t' = 42$, □ $t' = 98$ and △ $t' = 171$ experimental data of [46].

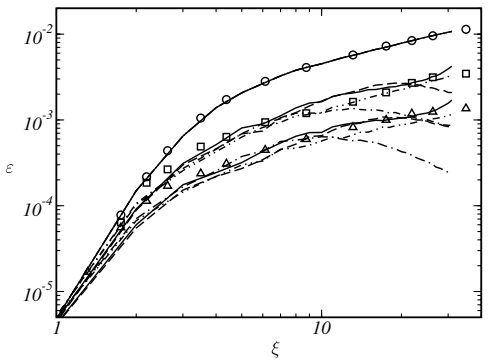

Fig. 8. Instantaneous 3D dissipation spectra for LES with 64^3 cells for the Comte-Bellot–Corrsin test case; ---- Chollet's eddy viscosity model, -·-·- Smagorinsky model, -···- dynamic Smagorinsky model, —— ALDM; ○ $t' = 42$, □ $t' = 98$ and △ $t' = 171$ experimental data of [46].

The conventional Smagorinsky model requires an ad hoc adjustment of C_S. The theoretical value is based on the assumption of a wide inertial range about ξ_C, i.e., a high-Reynolds-number spectrum, which is not the case in the CBC experiments. We found that a somewhat smaller C_S gives better results which are close to those of the dynamic Smagorinsky model. For the Chollet–Lesieur model with the eddy viscosity of Eq. (54) the overall results are similar to ALDM and the dynamic Smagorinsky model. At large wave numbers the energy drops and approaches that of the standard Smagorinsky model.

For the decay of total kinetic energy K, Fig. 9, we find $\partial K/\partial t \sim t^{-n}$ with $n = 1.25$. This corresponds to $\varepsilon = \partial K/\partial t \sim t^{-2.25}$ or $\varepsilon \sim K^{1.8}$. The exponent $n = 1.25$ is in a reasonable agreement with published experimental data [46,54,55] which range from $n = 1.2$ to $n = 1.3$.

Fig. 10 shows iso-surfaces of a constant vorticity magnitude at the last position. The threshold value is chosen to 3.5 times the mean vorticity. The visualization shows worm-like vorticity structures and indicates that ALDM reproduces basic mechanisms of turbulence. Even though Garnier et al. [11] investigated the inviscid Euler equation they obtained similar images using a threshold of 2.5 times the mean vorticity and a higher spatial resolution of 128^3 grid cells. The visual impression of the 64^3-point simulation of [11] can be reproduced when we filter our ALDM results to the effective resolution of 32^3, see Fig. 10.

4.4. Transition of the three-dimensional Taylor–Green vortex

One of the most demanding test cases for SGS models is laminar-turbulent transition. For the onset of transition the SGS model must not affect the instability modes of the laminar flow. Most eddy-viscosity models,

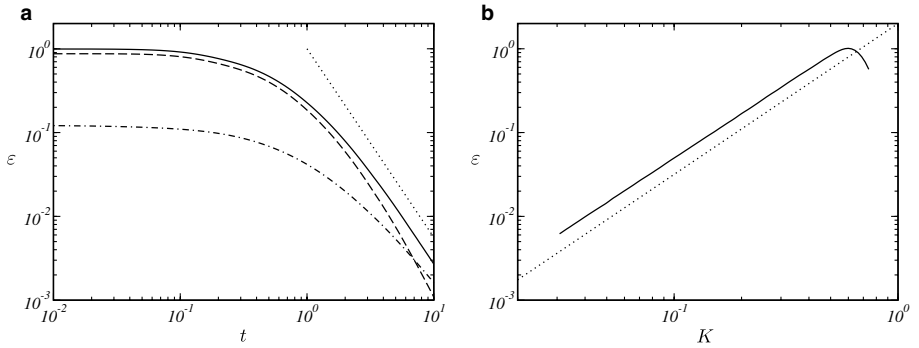

Fig. 9. Energy decay rate of ALDM results for decaying homogeneous isotropic turbulence for the Comte-Bellot–Corrsin experiment; (a) sources of dissipation; -·-·- molecular dissipation, ---- implicit SGS dissipation, —— total dissipation, ····· $\varepsilon \sim t^{-2.25}$; (b) —— total dissipation, power law ····· $\varepsilon \sim K^{1.8}$ (equivalent to $K \sim t^{-1.25}$).

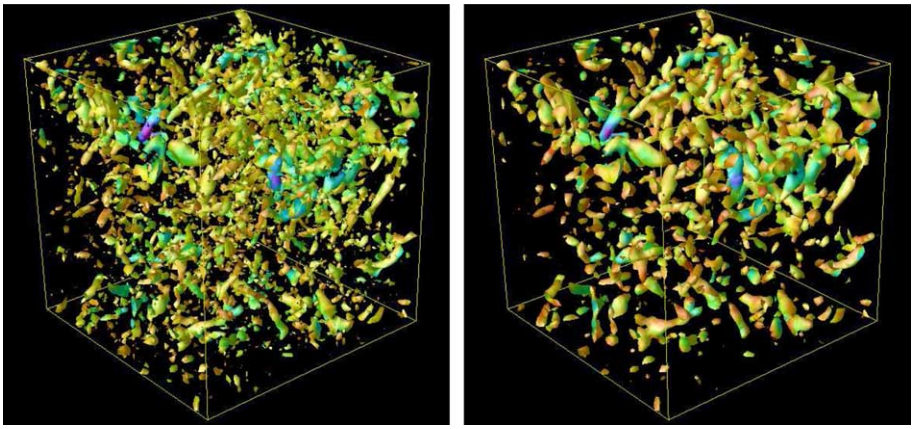

Fig. 10. Iso-surfaces of constant vorticity magnitude at the final station of the CBC experiment for implicit LES with ALDM. Left: original data from ALDM. Right: filtered with top-hat filter width 2Δ. Colors indicate kinetic energy.

for instance the Smagorinsky model and the structure-function model of Métais and Lesieur [8,41,56], do not satisfy this requirement without modifications.

A suitable test scenario for a periodic computational domain is the 3D Taylor–Green vortex (TGV). This flow is characterized by the initial data

$$\bar{\boldsymbol{u}}(t=0) \approx \boldsymbol{u}(t=0) = \begin{bmatrix} 0 \\ \cos(x)\sin(y)\cos(z) \\ -\sin(x)\cos(y)\sin(z) \end{bmatrix}. \tag{70}$$

At $t = 0$ the entire kinetic energy is contained within eight Fourier modes on the wave-number shell $\xi = \sqrt{3}$. At early times the TGV evolution is laminar and strongly anisotropic, see Fig. 11. Then energy is transferred to larger wave numbers by vortex stretching. Visualizations of vortices show that they roll up, divide and re-connect, see Fig. 11. Preserving spatial symmetries the flow eventually becomes turbulent. In the final steps, the small scales are nearly isotropic and exhibit an $\xi^{-5/3}$ inertial range of the kinetic-energy spectrum.

We compare our LES with DNS of Brachet et al. [58] which were originally performed on a grid of 256^3 modes and repeated with 864^3 modes about 10 years later [59]. These spectral simulations exploit spatial

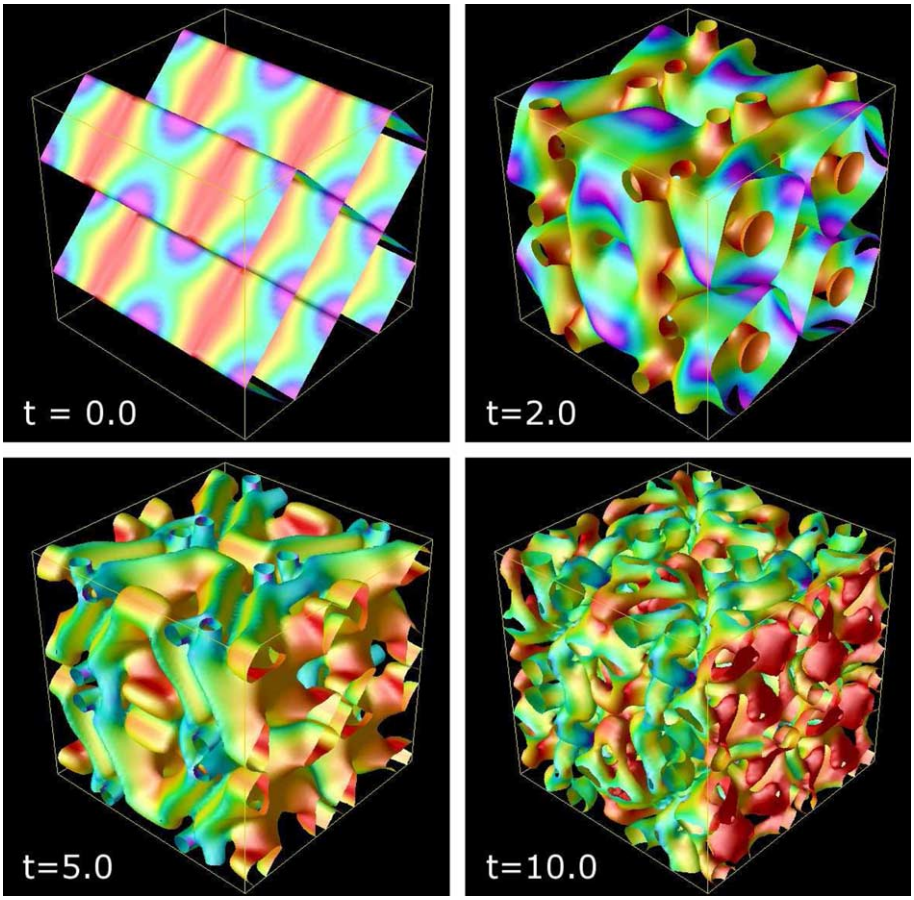

Fig. 11. Iso-surfaces for the zero Q-criterion (see [57]) for implicit LES of Taylor–Green vortex with ALDM at $Re = 400$. Colors indicate kinetic energy.

symmetries of the TGV to reduce the effective computational cost by a factor of 8. It was therefore possible to resolve Reynolds numbers up to $Re = 3000$ in [58].

For LES spatial symmetries are not imposed. The computational domain is a $(2\pi)^3$ box that contains 8 counter-rotating vortices. It is discretized with 64^3 cells and has periodic boundary conditions. To assess the quality of the LES the characteristic growth and decay of the dissipation rate is compared between LES using ALDM and the DNS of Brachet et al. [58, Fig. 7], see Fig. 12. The considered Reynolds numbers range from $Re = 100$ to $Re = 3000$. For an assessment of ALDM with respect to standard LES, we also show results for the conventional ($C_S = 0.18$) Smagorinsky model, the dynamic Smagorinsky model, and the Chollet–Lesieur model at the same resolution. To demonstrate the effect of the SGS models simulations without SGS model were performed. These simulations became unstable as soon as the energy transfer reached at the highest resolved wave numbers, see Fig. 12.

The Smagorinsky model with constant parameter C_S is obviously not well suited for transitional flows. Even in the fully resolved $Re = 100$ case excessive dissipation affects the flow evolution. At larger Re the conventional Smagorinsky model gives wrong dissipation rates and a completely wrong flow structure. If the Smagorinsky parameter is adjusted dynamically the behavior improves significantly. The SGS viscosity vanishes for laminar flow. The prediction is good for the two lowest Reynolds numbers throughout the entire time interval and up to $t = 8$ for $Re = 400$. An advantage of the Chollet–Lesieur model is that no energy is dissipated by the model in the early stages of the cascade, when no energy has yet reached at the cut-off wavenumber. At later stages, however, it is to dissipative.

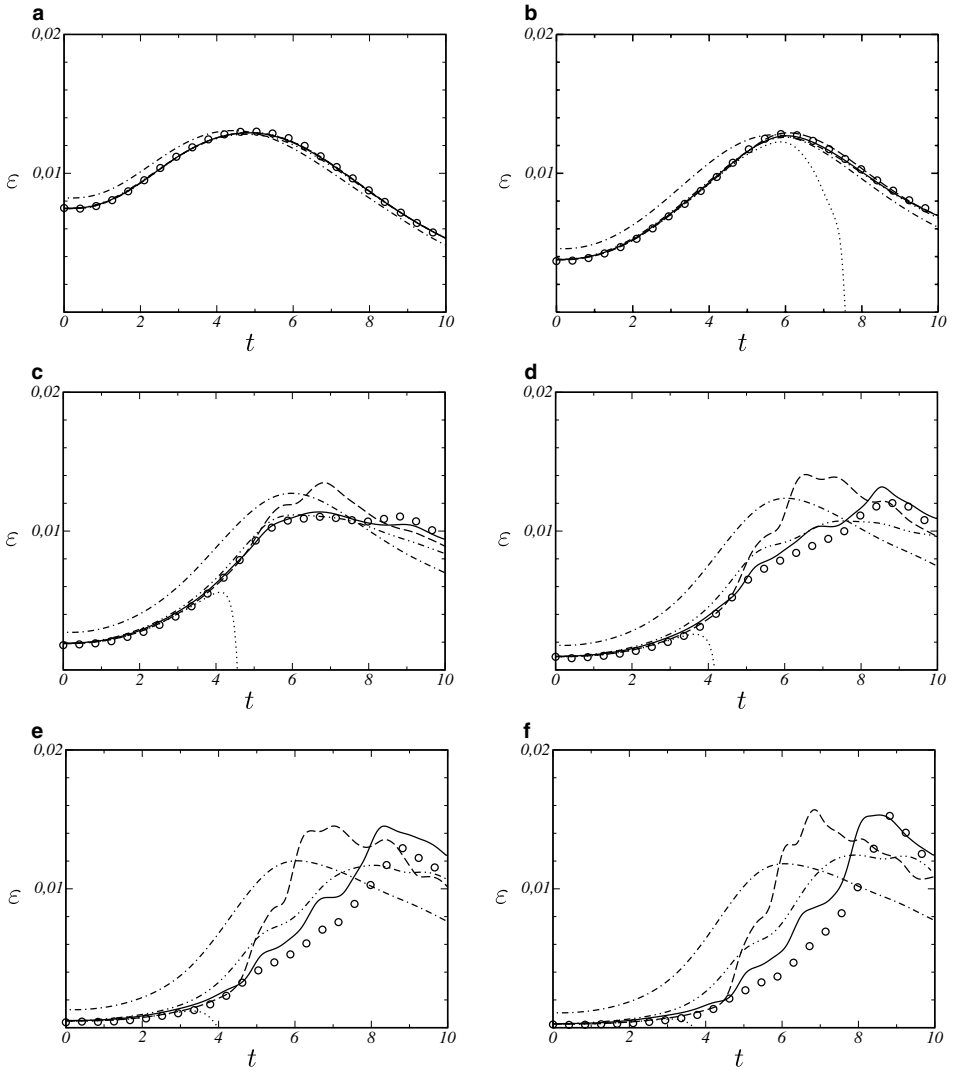

Fig. 12. Rate of energy dissipation for LES of the Taylor–Green vortex at Re = (a) 100, (b) 200, (c) 400, (d) 800, (e) 1600, (f) 3000; ····· without SGS model, ---- Chollet's eddy viscosity model, -·-·- Smagorinsky model, -···- dynamic Smagorinsky model, —— ALDM, ○ DNS data from [58].

Much better results are obtained with ALDM. The error increases with increasing Reynolds number but stays at all times significantly smaller than for the dynamic Smagorinsky model. Up to $Re = 800$ the difference between ALDM and DNS is negligibly small. Note that the resolution requirement of a DNS of $Re = 800$ is two orders of magnitude higher than that of the LES.

The dissipation as shown in Fig. 12 generally can originate from three sources. One source is molecular dissipation which is inversely proportional to the Reynolds number. The second source is transfer which is explicitly modeled by SGS dissipation. The third source is numerical dissipation which should be negligible for proper explicit SGS modeling. For implicit SGS modeling, however, the third source replaces the second one. This is the case with ALDM as shown in Fig. 13. At low Re discretization errors do not significantly contribute to dissipation. However, the implicit model activates itself with increasing Re and finally dominates the molecular dissipation at $Re = 3000$. These results for the TGV confirm that ALDM owing to its solution adaptivity over a large range of Reynolds numbers functions as intended.

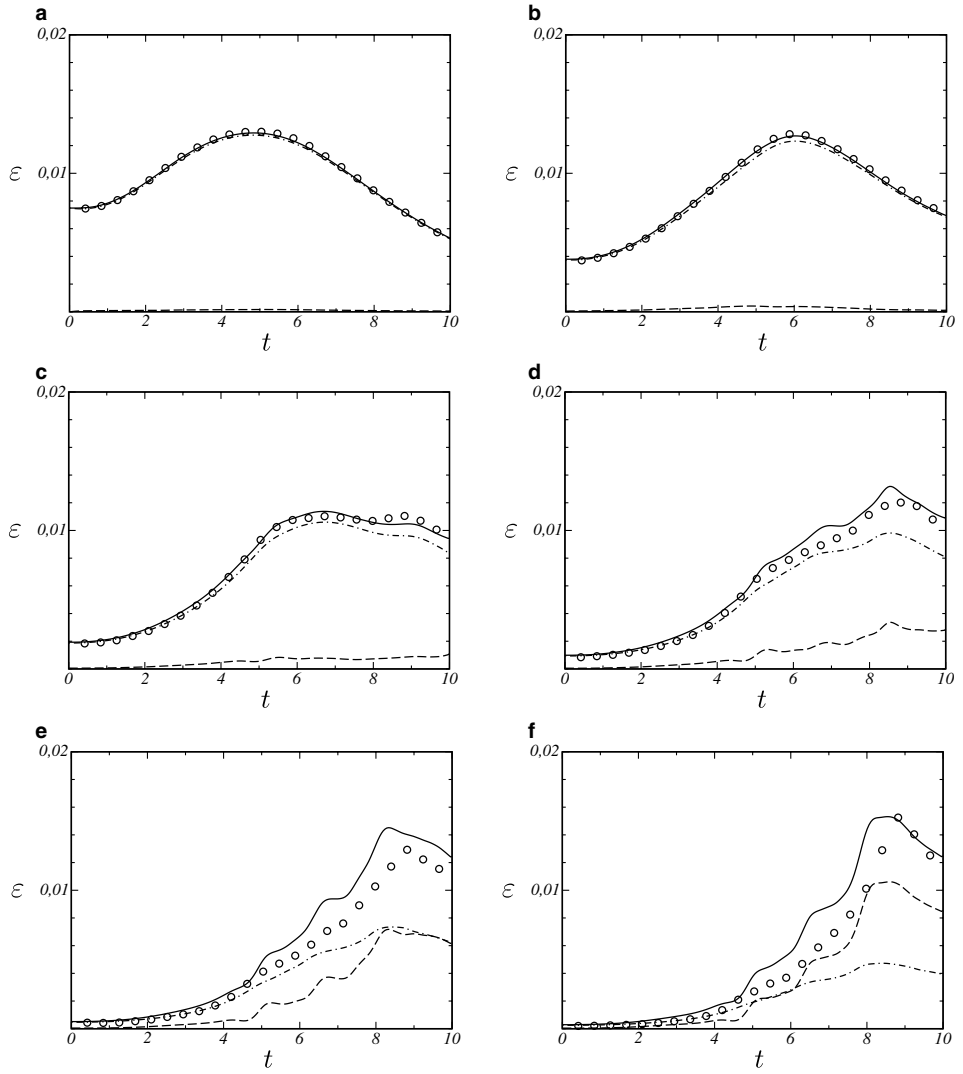

Fig. 13. Contributions to energy dissipation in ALDM for LES of the Taylor–Green vortex at $Re =$ (a) 100, (b) 200, (c) 400, (d) 800, (e) 1600, (f) 3000; -·-·- molecular dissipation, ---- implicit SGS dissipation, —— total dissipation, ○ DNS data from [58].

5. Conclusion

We have proposed a new approach to implicit LES of turbulent flows which we refer to as the adaptive local deconvolution method (ALDM). For this purpose, the concept of a solution-adaptive approximate deconvolution based on a formulation for 1D conservation laws [13] is developed for the incompressible 3D Navier–Stokes equations. With ALDM numerical discretization and SGS modeling are merged entirely. This is possible by exploiting the formal equivalence between cell-averaging and reconstruction in finite-volume discretizations and top-hat filtering and deconvolution in SGS-modeling. Instead of maximizing the order of accuracy, here deconvolution is regularized by limiting the degree of local interpolation polynomials and by permitting lower-order polynomials to contribute to the truncation error. Adaptivity of the deconvolution operator is achieved by weighting the respective contributions by an adaptation of WENO smoothness measures. The approximately deconvolved field is inserted into a consistent numerical flux function. Flux function and nonlinear weights introduce five model parameters. They allow to control the truncation error which provides the implicit SGS model.

Implicit SGS modeling requires systematic procedures for design and analysis of appropriate discretization schemes. For this purpose, the modified differential equation is analyzed in spectral space. Optimal model

parameters are determined by minimizing a cost function which measures the difference between spectral numerical viscosity and the eddy viscosity from EDQNM theory for isotropic turbulence.

The determined model parameters are kept unchanged for all subsequent a posteriori tests. The performance of the implicit model was evaluated by simulations of different flow configurations. Large-scale forced and decaying three-dimensional homogeneous isotropic turbulence were considered. For transitional flows the model performance was tested by an application to instability and breakdown of the 3D Taylor–Green vortex. For all test cases the implicit model shows an excellent agreement with theory and experimental data. It is demonstrated that ALDM performs at least as well as established explicit models. It should also be noted that the computational effort of the implicit model is comparable to the dynamic Smagorinsky model. The application of the proposed discretization scheme to wall bounded flows is subject of ongoing research and will be reported in a subsequent paper.

Acknowledgments

This research is supported by the German Research Council (Deutsche Forschungsgemeinschaft – DFG) in the framework of the French–German research group "LES of Complex Flows" (FG507). J.A. Domaradzki was supported by NSF and a research fellowship of the Alexander von Humboldt Foundation.

Appendix A. Evolutionary optimization

The employed automatic optimization algorithm follows an evolutionary strategy where set of free parameters is considered as genome of an individual. The algorithm operates on a population of individuals and applies the survival-of-the-fittest principle. At each generation, a new set of individuals is created by selection according to the level of fitness, recombination, and random mutation. This process leads to the evolution of a population of individuals that is better adapted to a cost function than the population that it was created from. Since this algorithm works on populations instead of single individuals, the search is performed in an efficient parallel manner. For further details, the reader is referred to [60–62] and the references therein.

For parameter evaluation and optimization, we perform LES of isotropic homogeneous turbulence at an infinite computational Reynolds number. The $(2\pi)^3$-periodic computational domain is discretized with 32^3 cells. The time-step size is adjusted according to Eq. (61) with CFL = 1.0. This Courant number is identical to that used in all other simulations. Ten initial velocity fields are obtained by filtering and truncating data from separate simulations with a dynamic Smagorinsky SGS model with 128^3 cells.

The cost function used for evaluating a set of the discretization parameters of ALDM is

$$\mathscr{C}\left(\gamma_{2,0}^{+1/2},\gamma_{3,0}^{+1/2},\gamma_{3,1}^{+1/2},\gamma_{3,1}^{0},\sigma\right)=\sqrt{\frac{1}{\xi_C-1}\sum_{\xi^+=2/\xi_C}^{1}\left(\left\langle \nu_{\mathrm{num}}^{+}(\xi^+)\right\rangle-\nu_{\mathrm{Chollet}}^{+}(\xi^+)\right)^2}.$$

It is computed by averaging the numerical viscosity spectra from 10 independent simulations, see Sections 3.2 and 3.3 for details. Each realization is advanced by only 1 time step so that computational cost amounts to 10 time steps per evaluated individual.

Performance and convergence of the employed optimization algorithm depend on the mutation model. We employ normally distributed random numbers. The variance is initially set to $\sigma_{\mathrm{mut}}^2=0.1$ and updated by a factor of $0.95^{\pm1}$ after every generation, where successful mutations enlarge the target area and unsuccessful mutations make it smaller. For further details on the algorithm see Table A.1.

Normally, distributed random numbers are used as an initial guess for the first population. The subsequent generation is created by a four-step algorithm consisting of parent selection, recombination, mutation, and new-population selection. This scheme is iterated until a maximum number of generations is reached. The final set of parameters which was selected after evaluating 200 generations is given in Table A.1. The convergence of the optimization algorithm is demonstrated by comparing the best 50 sets, the best 200 sets, and all tested sets of parameters in Table A.2.

Table A.1
Parameters of the evolutionary optimization algorithm

Parameter	Value
Number of genes per individual	5
Initialization	Random numbers, equally distributed on [0,0.3333)
Number of generations	200
Population	50
Offspring per generation	40
Selection of parents	Tournament
Offspring generation	Arithmetic cross-over and mutation
Mutation model	Normal distribution with zero mean
Initial mutation variance	0.1
Mutation-variance update factor	0.95
Admissible parameter range	[0.0,1.0]
Admissible mutation-variance range	$[10^{-6},10^{+3}]$

Table A.2
Mean values and SD of cost function and parameter values demonstrate the convergence of the evolutionary optimization algorithm

Parameter	Best 50 individuals	Best 200 individuals	All evaluated individuals
$\mathscr{C}$	0.0054860 ± 0.0000004	0.0054878 ± 0.0000071	0.2377798 ± 3.6380424
$\gamma_{3,1}^{0}$	0.0501310 ± 0.0001948	0.0501456 ± 0.0003782	0.0652569 ± 0.1125736
$\gamma_{2,0}^{+1/2}$	1.0000000 ± 0.0000000	1.0000000 ± 0.0000000	0.9741133 ± 0.1789786
$\gamma_{3,0}^{+1/2}$	0.0845990 ± 0.0001628	0.0847430 ± 0.0010236	0.1221711 ± 0.2100462
$\gamma_{3,1}^{+1/2}$	0.0189470 ± 0.0001435	0.0186506 ± 0.0013708	0.0289264 ± 0.1117276
σ	0.0689194 ± 0.0000965	0.0689116 ± 0.0001884	0.0664319 ± 0.0947205

References

[1] A. Leonard, Energy cascade in large eddy simulations of turbulent fluid flows, Adv. Geophys. 18A (1974) 237–248.
[2] A.A. Aldama, Filtering Techniques for Turbulent Flow Simulation, Lecture Notes in Engineering, vol. 56, Springer, Berlin, 1990.
[3] V.M. Dakhoul, K.W. Bedford, Improved averaging method for turbulent flow simulation. I – Theoretical development and application to Burgers' transport equation, Int. J. Numer. Meth. Fluids 6 (1986) 49–64.
[4] C.D. Pruett, T.B. Gatski, C.E. Grosch, W.D. Thacker, The temporally filtered Navier–Stokes equations: properties of the residual stress, Phys. Fluids 15 (2003) 2127–2140.
[5] C.D. Pruett, B.C. Thomas, C.E. Grosch, T.B. Gatski, A temporal approximate deconvolution model for LES, in: J.A.C. Humphrey, T.B. Gatski, J.K. Eaton, R. Friedrich, N. Kasagi, M.A. Leschziner (Eds.), Fourth International Symposium on Turbulence and Shear Flow Phenomena, Williamsburg, VA, USA, 2005, pp. 705–710.
[6] J.A. Domaradzki, N.A. Adams, Direct modeling of subgrid scales of turbulence in large-eddy simulations, J. Turb. 3 (2002) 24.
[7] P. Sagaut, Large-Eddy Simulation for Incompressible Flows, second ed., Springer, Berlin, 2002.
[8] M. Lesieur, Turbulence in Fluids, third ed., Kluwer Academic Publishers, Dordrecht, The Netherlands, 1997.
[9] S. Ghosal, An analysis of numerical errors in large-eddy simulations of turbulence, J. Comput. Phys. 125 (1996) 187–206.
[10] P.S. Zandonade, J.A. Langford, R.D. Moser, Finite-volume optimal large-eddy simulation of isotropic turbulence, Phys. Fluids 16 (7) (2004) 2255–2271.
[11] E. Garnier, M. Mossi, P. Sagaut, P. Comte, M. Deville, On the use of shock-capturing schemes for large-eddy simulation, J. Comput. Phys. 153 (1999) 273–311.
[12] F.F. Grinstein, C. Fureby, From canonical to complex flows: recent progress on monotonically integrated LES, Comp. Sci. Eng. 6 (2004) 36–49.
[13] N.A. Adams, S. Hickel, S. Franz, Implicit subgrid-scale modeling by adaptive deconvolution, J. Comput. Phys. 200 (2004) 412–431.
[14] C. Fureby, G. Tabor, H.G. Weller, A.D. Gosman, A comparative study of subgrid scale models in homogeneous isotropic turbulence, Phys. Fluids 9 (1997) 1416–1429.
[15] L.G. Margolin, W.J. Rider, A rationale for implicit turbulence modeling, Int. J. Numer. Meth. Fluids 39 (2002) 821–841.
[16] R. Vichnevetsky, J.B. Bowles, Fourier Analysis of Numerical Approximations of Hyperbolic Equations, SIAM, Philadelphia, 1982.
[17] J.-P. Chollet, Two-point closures as a subgrid-scale modeling tool for large-eddy simulations, in: F. Durst, B.E. Launder (Eds.), Turbulent Shear Flows IV, Springer, Heidelberg, 1984, pp. 62–72.
[18] J.A. Domaradzki, Z. Xiao, P.K. Smolarkiewicz, Effective eddy viscosities in implicit large eddy simulations of turbulent flows, Phys. Fluids 15 (2003) 3890–3893.
[19] U. Schumann, Subgrid scale model for finite-difference simulations of turbulence in plane channels and annuli, J. Comput. Phys. 18 (1975) 376–404.

[20] J.A. Langford, R.D. Moser, Breakdown of continuity in large-eddy simulation, Phys. Fluids 13 (2001) 1524–1527.
[21] A. Harten, B. Engquist, S. Osher, S. Chakravarthy, Uniformly high order accurate essentially non-oscillatory schemes, III, J. Comput. Phys. 71 (1987) 231–303.
[22] C.-W. Shu, Essentially non-oscillatory and weighted essentially non-oscillatory schemes for hyperbolic conservation laws, Tech. Rep. 97-65, ICASE, NASA Langley Research Center, Hampton, VA, 1997.
[23] S.W. Liu, C. Meneveau, J. Katz, On the properties of similarity subgrid-scale models as deduced from measurements in a turbulent jet, J. Fluid Mech. 275 (1994) 83–119.
[24] G.-S. Jiang, C.-W. Shu, Efficient implementation of weighted ENO schemes, J. Comput. Phys. 126 (1996) 202–228.
[25] R.J. LeVeque, Numerical Methods for Conservation Laws, Birkhäuser, Basel, Switzerland, 1992.
[26] U. Frisch, Turbulence, Cambridge University Press, Cambridge, 1995.
[27] C. Fureby, F.F. Grinstein, Large eddy simulation of high-Reynolds-number free and wall-bounded flows, J. Comput. Phys. 181 (2002) 68–97.
[28] L.G. Margolin, W.J. Rider, The design and construction of implicit LES models, Int. J. Numer. Meth. Fluids 47 (2005) 1173–1179.
[29] G.K. Batchelor, The Theory of Homogenous Turbulence, Cambridge University Press, Cambridge, 1953.
[30] S.B. Pope, Turbulent Flows, Cambridge University Press, Cambridge, 2000.
[31] J.-P. Chollet, M. Lesieur, Parametrization of small scales of three-dimensional isotropic turbulence utilizing spectral closures, J. Atmos. Sci. 38 (1981) 2747–2757.
[32] W. Heisenberg, Zur statistischen Theorie der Turbulenz, Z. Phys. 124 (1946) 628–657.
[33] S. Hickel, S. Franz, N. Adams, P. Koumoutsakos, Optimization of an implicit subgrid-scale model for LES, in: Proceedings of the 21st International Congress of Theoretical and Applied Mechanics, Warsaw, Poland, 2004.
[34] U. Piomelli, W.H. Cabot, P. Moin, S. Lee, Subgrid-scale backscatter in turbulent and transitional flows, Phys. Fluids 3 (1991) 1766–1771.
[35] D.C. Leslie, G.L. Quarini, The application of turbulence theory to the formulation of subgrid modelling procedures, J. Fluid Mech. 91 (1979) 65–91.
[36] J.A. Domaradzki, E.M. Saiki, Backscatter models for large-eddy simulation, Theor. Comput. Fluid Dyn. 9 (1997) 75–83.
[37] D. Carati, S. Ghosal, P. Moin, On the representation of backscatter in dynamic localization models, Phys. Fluids 7 (1995) 606–616.
[38] C.-W. Shu, Total-variation-diminishing time discretizations, SIAM J. Sci. Stat. Comput. 9 (6) (1988) 1073–1084.
[39] S. Gottlieb, C.-W. Shu, Total variation diminishing Runge–Kutta schemes, Math. Comput. 67 (1998) 73–85.
[40] V.A. Titarev, E.F. Toro, Finite-volume WENO schemes for three-dimensional conservation laws, J. Comput. Phys. 201 (2004) 238–260.
[41] O. Métais, M. Lesieur, Spectral large-eddy simulations of isotropic and stably-stratified turbulence, J. Fluid Mech. 239 (1992) 157–194.
[42] J.A. Domaradzki, R.W. Metcalfe, R.S. Rogallo, J.J. Riley, Analysis of subgrid-scale eddy viscosity with use of results from direct numerical simulations, Phys. Rev. Lett. 58 (1987) 547–550.
[43] W.D. McComb, The Physics of Fluid Turbulence, Clarendon Press, Oxford, 1990.
[44] X. Yang, J.A. Domaradzki, Large eddy simulations of decaying rotating turbulence, Phys. Fluids 16 (11) (2004) 4088–4104.
[45] P.K. Yeung, Y. Zhou, On the universality of the Kolmogorov constant in numerical simulations of turbulence, Tech. Rep. 97-64, ICASE, NASA Langley Research Center, Hampton, VA, 1997.
[46] G. Comte-Bellot, S. Corrsin, Simple Eulerian time correlation of full and narrow-band velocity signals in grid-generated 'isotropic' turbulence, J. Fluid Mech. 48 (1971) 273–337.
[47] A. Misra, T.S. Lund, Evaluation of a vortex-based subgrid stress model using DNS databases, in: CTR Proceedings of 1996 Summer Program, Center for Turbulence Research, Stanford University and NASA Ames Research Center, Stanford, CA, 1996, pp. 359–368.
[48] S. Ghosal, T.S. Lund, P. Moin, K. Akselvoll, A dynamic localization model for large-eddy simulation of turbulent flows, J. Fluid Mech. 286 (1995) 229–255.
[49] J. Smagorinsky, General circulation experiments with the primitive equations, Mon. Weath. Rev. 93 (1963) 99–164.
[50] D.K. Lilly, On the application of the eddy viscosity concept in the inertial subrange of turbulence, NCAR MS 123, National Center for Atmospheric Research, Boulder, CO, 1966.
[51] D.K. Lilly, The representation of small-scale turbulence in numerical simulation experiments, in: H.H. Goldstein (Ed.), Proceedings of the IBM Scientific Computing Symposium on Environmental Sciences, IBM, 1967, pp. 195–201.
[52] M. Germano, U. Piomelli, P. Moin, W.H. Cabot, A dynamic subgrid-scale eddy viscosity model, Phys. Fluids A 3 (1991) 1760–1765.
[53] D.K. Lilly, A proposed modification of the Germano subgrid-scale closure model, Phys. Fluids A 4 (1992) 633–635.
[54] AGARD, A Selection of Test Cases for the Validation of Large-Eddy Simulations of Turbulent Flows, Technical Report AGARD-AR-345, NATO, 1998.
[55] H.S. Kang, S. Chester, C. Meneveau, Decaying turbulence in an active-grid-generated flow and large-eddy simulation, J. Fluid Mech. 480 (2003) 129–160.
[56] M. Lesieur, O. Métais, New trends in large-eddy simulations of turbulence, Annu. Rev. Fluid. Mech. 28 (1996) 45–82.
[57] J. Jeong, F. Hussain, On the identification of a vortex, J. Fluid Mech. 285 (1995) 69–94.
[58] M. Brachet, D. Meiron, S. Orszag, B. Nickel, R. Morf, U. Frisch, Small-scale structure of the Taylor–Green vortex, J. Fluid Mech. 130 (1983) 411–452.
[59] M. Brachet, M. Meneguzzi, A. Vincent, H. Politano, P.-L. Sulem, Numerical evidence of smooth self-similar dynamics and possibility of subsequent collapse for three-dimensional ideal flow, Phys. Fluids 4 (1992) 2845–2854.
[60] T. Back, D.B. Fogel, Z. Michalewicz, Handbook of Evolutionary Computation, University Oxford Press, Oxford, 1997.
[61] D. Beasley, D.R. Bull, R.R. Martin, An overview of genetic algortihms: Part 1, fundamentals, Univ. Comput. 15 (1993) 58–69.
[62] D. Beasley, D.R. Bull, R.R. Martin, An overview of genetic algortihms: Part 2, research topics, Univ. Comput. 15 (1993) 170–181.